Preprint – Accepted for publication in *Bulletin of Volcanology*
Citation: Angarita, M., Grapenthin, R., Tan, P.K.D., Saunders-Shultz, P., Girona, T., Parameswaran, R.M., Lopez, T.M., Izbekov, P.E., Fee, D., Burgos, V., Moshrefzadeh, J.A., Shreve, T., and Larsen, J. (in press). Multidisciplinary perspectives on Shishaldin Volcano: an open-system, deforming volcano. Bulletin of Volcanology. https://doi.org/10.1007/s00445-026-01970-0

Multidisciplinary perspectives on Shishaldin Volcano: An open-system, deforming volcano

Mario Angarita[1,2*], Ronni Grapenthin[1], Darren Tan[1,3], Pablo Saunders-Shultz[1,4], Társilo Girona[1,5], Revathy M. Parameswaran[6], Taryn M. Lopez[1], Pavel E. Izbekov[1], David Fee[1], Vanesa Burgos[1,7], Jamshid A. Moshrefzadeh[8], Tara Shreve[1,9], Jessica F. Larsen[1]

[1]Alaska Volcano Observatory and Geophysical Institute, University of Alaska Fairbanks, AK, USA.
[2]Now at Alaska Satellite Facility, University of Alaska Fairbanks, AK, USA.
[3]Now at Earthquake Research Institute, University of Tokyo, Tokyo, Japan.
[4]Now at Alaska Volcano Observatory, US Geological Survey, Anchorage, AK, USA.
[5]Now at Geosciences Barcelona (GEO3BCN), Consejo Superior de Investigaciones Científicas, Barcelona, Spain.
[6]Geophysical Institute, University of Alaska, Fairbanks, AK, USA.
[7]Now at Centro Geofísico de Canarias, Instituto Geográfico Nacional de España, Santa Cruz de Tenerife, Spain.
[8]Mineral Resources team,Alaska Division of Geological and Geophysical Surveys, Fairbanks, AK, USA.
[9]Now at Department of Natural Resources, Utah Geological Survey, Salt Lake City, UT, USA.

*Corresponding author(s). E-mail(s): mfangaritasr@alaska.edu;

Abstract

The integration of multidisciplinary data across multiple eruptions is essential to improve our understanding of a volcanic system. Shishaldin Volcano is one of the most active volcanoes in Alaska, with several reported eruptions over the last 300 years. We synthesize multidisciplinary datasets going back to 1997, and focus our

analyses on the 2014–15, 2019–20, and 2023 eruptive periods. We find pronounced periods of volcanic tremor, long-period and volcano-tectonic seismicity; thermal anomalies with a radiative power ranging from 10–1000 MW; 1–2 °C increase in the median, low-pass filtered thermal anomaly; SO_2 emission rates ranging from 30–287 kt/yr; and previously unrecognized surface deformation that includes two episodes of $\sim$ 1 cm/yr inflation preceding the 2014–15 and the 2019–20 eruptions, and deflation prior to, during, and after the 2023 eruption in the GNSS records. The new ground-based geodetic observations allow us to refine previous interpretations of the magmatic plumbing system. Borehole tilt records are best explained by a shallow, 1–1.5 km long conduit centered at sea level with a radius of 150 m. From the GNSS records, we find a pressurized sphere between 2–4 km below sea level (bsl) depth, and a 10 km long conduit centered at $\sim$ 6 km bsl depth as the most probable inflation and deflation sources, respectively. We propose that the observed seismicity at a nearby fault system can be explained by magma/fluid flow among our resolved magma sources, that modulate the local stress field. We integrate these models and observations into a conceptual magma system model, building upon previous findings for Shishaldin Volcano.

Keywords: Shishaldin Volcano, multidisciplinary synthesis, open-system deforming volcano, magma system model, volcano monitoring

1 Introduction

It is broadly recognized that a comprehensive understanding of volcanic processes requires the analysis, interpretation and synthesis of multidisciplinary data, ideally across multiple eruptions (e.g., NASEM, 2017). This has been demonstrated by past efforts that led to advances, for instance, at Galeras volcano, Colombia, where correlations between SO_2 flux and long-period seismicity have been used to interpret gas movement from the magma body to the surface and thus monitor the pre-eruptive pressure buildup (Fischer et al., 1994). Similarly, joint analysis of satellite SO_2 measurements and deformation data improved our understanding of magma compressibility at Chaiten volcano, Chile, and Okmok caldera, Alaska (Kilbride, Edmonds, & Biggs, 2016). Gudmundsson et al. (2016) combined Interferometric Synthetic Aperture Radar (InSAR), Global Navigation Satellite System (GNSS), Multi-GAS measurements, ice surface topography changes, gravity profiles, thermobarometry observations, seismicity, and element compositions of minerals and glasses to find that the collapse of Bárdarbunga caldera, Iceland was caused by lateral magma transport from its magma reservoir to the Holuhraun lava field, causing the 2014–15 eruption. These cases highlight the potential to gain deep insights into volcanic systems through retrospective analysis of multidisciplinary datasets using new tools.

Motivated by the successes of such multidisciplinary data syntheses, we synthesize, reanalyze, and reinterpret available data for Shishaldin (Aleut: Sisquk or Sisagux) Volcano (2857 m), a prolific volcano in the Aleutian Arc with frequent, well-observed eruptions between 1997–2024 (Orr et al., 2023). We revisit Shishaldin's recent eruptions from 2014–15, 2019–20, and 2023, which exhibited a range of effusive and explosive activity. By applying a suite of new tools to analyze data from these eruptions, we add observations that allow us to reevaluate and revise past conceptual models and hypotheses about Shishaldin's magmatic system. Specifically, using newly resolved GNSS displacements, we constrain the most probable magmatic sources and we utilize tilt observations to infer conduit dynamics. We discuss possible mechanisms that explain the multidisciplinary observations from the three eruptive periods, including interactions between the magmatic system and a nearby tectonic fault system located less than 3 km west of the edifice. We then combine these results with observations and models from seismic, thermal, and SO_2 datasets to develop a new conceptual model for Shishaldin's magmatic system.

2 Geologic background and eruptive history

Shishaldin is the highest stratovolcano on Unimak Island in the Eastern Aleutian Islands of Alaska (Figure 1). The summit cone is thought to have largely been built over the last 10 ka on top of a glaciated volcanic caldera and shield (Fournelle, 1988). The main geologic units are historic ($<$ 200 years), and from the Holocene, Pleistocene and late Pliocene.

In historical reports, steam or "smoke" has been noticed at the summit, with volcanic activity reported since 1775. Historical records, direct observations, and recent satellite imagery document multiple eruptions in the 19th and 20th centuries (McGimsey & Neal, 1996; Reeder, 1990; Shackelford, 1978; Siebert, Simkin, & Kimberly, 2010). The most recent eruptions in 1999, 2014–15, 2019–20, and 2023 were instrumentally observed.

Leading up to the 1999 eruption, the Alaska Volcano Observatory (AVO) detected precursory activity including thermal anomalies, steam and ash plumes, and low-frequency seismicity. The seismic activity gradually increased after a shallow M_L 5.2 tectonic earthquake ∼14 km west of Shishaldin's summit on March 4, 1999. The main phase of the eruption started on April 19, 1999, when a sub-Plinian plume rose above 16 km above sea level (asl) over an 80-minute period, followed by a Strombolian phase that lasted three days (Nye et al., 2002). AVO increased the Aviation Color Code (ACC) and Volcanic Alert Level (VAL) from GREEN/NORMAL to YELLOW/ADVISORY during periods volcanic unrest on February 2–18, 2000; May 3–September 24, 2004; January 6–February 20, 2009; and July 10–October 19, 2009 (McGimsey, Neal, Girina, Chibisova, & Rybin, 2014; Neal, McGimsey, & Chubarova, 2004; Neal, McGimsey, Dixon, & Melnikov, 2005).

After 14 years of eruptive quiescence, satellite data showed increases in the surface temperature in the summit crater in January 2014, prompting AVO to increase the ACC/VAL from GREEN/NORMAL to YELLOW/ADVISORY. The activity increased in February with intermittent tremor and airwave explosion signals recorded by infrasound instruments. The eruptive episode began in March 2014. Satellite data indicated temperatures in the summit crater consistent with lava extrusion, resulting in AVO raising the ACC/VAL to ORANGE/WATCH. In the following months, explosions and seismic unrest were detected, accompanied by steaming and occasional ash plumes (C.E. Cameron et al., 2017). However, lava was only present in the summit crater with no reports of lava flows or lahars on the flanks (C.E. Cameron et al., 2017). By November 2015, temperatures and steaming had decreased significantly. AVO lowered the ACC/VAL to YELLOW/ADVISORY (Dixon, Cameron, & Wallace, 2017). Without further evidence of lava in the crater, AVO considered the eruption over by March 2016 (C. Cameron et al., 2020).

On July 1, 2019, satellite imagery indicated elevated surface temperatures, and the seismic network detected tremor and LP earthquakes as early as mid-June. On July 13, increased amplitude of seismic tremor, elevated surface temperatures, and reports of incandescence within the summit crater prompted AVO to raise the ACC/VAL to YELLOW/ADVISORY and then to ORANGE/WATCH on July 23 after AVO field crews reported active lava within the summit crater. On September 19, the lava present in the vent disappeared into the conduit and satellite imagery reported lower temperatures, leading AVO to downgrade the ACC/VAL to YELLOW/ADVISORY on September 26. Activity resumed with the appearance of a new spatter cone observed in satellite imagery on October 17, leading AVO to raise the ACC/VAL to

ORANGE/WATCH. The activity then escalated, with Strombolian explosions, lava fountaining, and lava flowing down the edifice flanks, resulting in melting ice and snow that formed lahars reaching the Bering Sea (Orr et al., 2023). Activity became explosive in January 2020, with three paroxysms on January 3, 7, and 20. After a brief pause, the ACC/VAL was lowered to YELLOW/ADVISORY on February 17 but raised again to ORANGE/WATCH on March 15 when satellite imagery indicated that lava was erupting within the summit crater. Small Strombolian explosions were detected by infrasound through late March. Activity declined in April, and AVO lowered the alert level to YELLOW/ADVISORY on April 16 and to GREEN/NORMAL on June 24 as activity returned to background levels (Orr et al., 2024).

The 2023 eruption produced 13 explosive events. Unrest was noticed in March 2023 with the detection of intermittent seismic tremor (Fee et al., This issue) and an SO_2 detection on April 5, 2023 (Lopez, Kelly, Lerner, & Rasmussen, This issue). In July, elevated temperatures were observed in satellite data and low-frequency earthquakes were detected by the seismic network, prompting AVO to raise the ACC/VAL from GREEN/NORMAL to YELLOW/ADVISORY on July 11 (Loewen, This issue). On the following day, the ACC/VAL was raised to ORANGE/WATCH after observing SO_2 detections and incandescence in the crater. The paroxysmal phase initiated on July 14, producing ash plumes up to 12 km asl (Gomez-Patron, Dietterich, & Schneider, This issue), and volcanic mudflows on the north flank. Additional paroxysms with notable plumes occurred between July and September (6–15 km asl). Several collapse events were observed starting on August 28, becoming more frequent during subsequent paroxysms. For example, lava fountaining on October 2 was followed by an explosive plume that reached 11 km asl and resulted in steaming, crater collapses, pyroclastic flows, and lahars. The last major eruptive event occurred on November 2, with an ash plume below 7 km asl. Smaller explosions and collapses continued for about a week. On January 2, 2024, AVO lowered the ACC/VAL to YELLOW/ADVISORY. Small collapse events, steaming and occasional SO_2 detections, and elevated seismicity and infrasound continued into July/August 2024. On August 30, 2024, AVO lowered the ACC/VAL to GREEN/NORMAL (Loewen, This issue). SO_2 emissions and weak infrasound signals continue to be detected at the time of this writing.

3 Prior Work

Insights from the 1999 eruption have dominated the conceptual understanding of Shishaldin, suggesting that the volcano is a non-deforming, open-system volcano, that we define here as a system with permanent or semipermanent conduits (Chaussard, Amelung, & Aoki, 2013) with no long-term shallow magma storage (< 10 km bsl).

3.1 Geology and Petrology

The predominant eruptive products of Shishaldin volcano are high alumina basalts, which, according to Fournelle (1988), may represent primary, mantle-derived magmas. If this interpretation is correct, Shishaldin likely possesses a mature magmatic plumbing system with an insulated conduit that permits the ascent of mantle-derived

magmas with minimal wall-rock contamination and limited crystal fractionation (Fournelle & Marsh, 1991).

According to chemical comparisons of glass in olivine-hosted melt inclusions with groundmass glasses, magma was largely degassed prior to the 1999 eruption (Stelling et al., 2002). These comparisons indicated that the magma resided in a short-lived shallow reservoir long enough to grow olivine phenocrysts (Stelling et al., 2002). Tephra deposit samples from the same eruption showed evidence of magma mixing up to $\sim$ 9 months before the eruption based on diffusion profiles of zoned olivine crystals (Rasmussen et al., 2018).

3.2 Seismology and Infrasound

Seismic unrest for the 1999 eruption began in January 1999, intensified in April 1999 and declined by May 1999. In the run-up sequence, seismic tremor was first detected on January 9, 1999, before growing stronger on February 9, 1999. Seismicity again intensified after the March 4 M_L 5.2 earthquake (Figure 1), which produced $\sim$ 900 aftershocks. Moran, Stihler, and Power (2002), assuming a dike opening beneath Shishaldin's vent, found that earthquake locations congregated in a zone where Coulomb stress increased, suggesting a possible connection between the tectonic and volcanic activity. The eruption eventually escalated into paroxysms on April 19, 1999, and April 22–23, 1999, seismically manifesting mostly as tremor.

In the years following the 1999 eruption, seismicity was characterized by the near-continuous occurrence of long-period (LP) and shallow ($<$ 4 km bsl) short-period (SP) earthquakes. Caplan-Auerbach and Petersen (2005) investigated these signals following a seismic swarm that had occurred between March and October 2002. They proposed a model which associated SP earthquakes with fluid moving within the conduit around an obstruction, and LP earthquakes with the coalescence of shallow gas bubbles. These seismic swarms persisted into 2003 and 2004. Petersen, Caplan-Auerbach, and McNutt (2005) estimated that the earthquakes concentrated between 0–3 km bsl depth. They related the LP signals in these swarms with puffs in the steam plume that remained after the eruption. Petersen (2007) also analyzed the swarms between 2001 and 2004 using waveform cross-correlation, and revealed that the swarms are primarily composed of one large event family. This event family was then linked to a choked flow model, where shock waves generated below a constriction produce pressure transients that excite the resonance of fluid filled crack (Chouet, 1988). Aside from the choked flow model, Cusano, Palo, and West (2015) investigated the polarization angle of LP signals between October 2003 and July 2004. They suggested that temporal variations in LP polarization dip are associated with changes in the depth at which gas nucleation occurs within the conduit. These depth variations could have been driven by magma intruding from a deeper source ($>$ 10 km bsl) to a shallower source ($<$ 5 km bsl) (Cusano et al., 2015).

3.3 Geodesy

The first geodetic observation of activity at Shishaldin is the InSAR-detected deformation from the March 4, 1999 M_L 5.2 earthquake (Lu & Dzurisin, 2014; Moran, Kwoun, Masterlark, & Lu, 2006). Moran et al. (2006) detected no deformation related to magmatic processes before or during the 1999 eruption and infer that deformation produced by a shallow (1–2 km bsl depth) source would not be observable due to SAR incoherence on the edifice. They could, thus, not rule out shallow summit deformation that might be detectable with more sensitive geodetic techniques. Furthermore, the deformation gradient produced by a deep source (>10 km bsl) was not observable by SAR missions available at the time due to the limited landmass of Unimak Island. Lu and Dzurisin (2014) extended the InSAR observations until 2010 and reached similar conclusions to Moran et al. (2006), finding no significant deformation. They estimated that InSAR would detect deformation at Shishaldin for volume changes $>5\,\mathrm{Mm}^3$ for a point source at 0–3 km bsl depth.

4 Data and Results

We collect, analyze, and compare multidisciplinary data going back to 1997 when the seismic network at Shishaldin became operational. This includes seismic data, earthquake catalogs, mid-infrared and thermal-infrared imagery acquired from the Moderate Resolution Imaging Spectroradiometer (MODIS) and Visible Infrared Imaging Radiometer Suite (VIIRS) satellite missions between 2000 and 2024, GNSS and tiltmeter records since 2008, and SO_2 emission rates from the Fioletov et al. (2023) and AVO (Lopez et al., This issue) catalogs. We summarize these observations together with the Aviation Color Code in Figure 2. The following subsections describe the data sources, analyses, and main findings for the geodetic, thermal, gas, and seismic datasets.

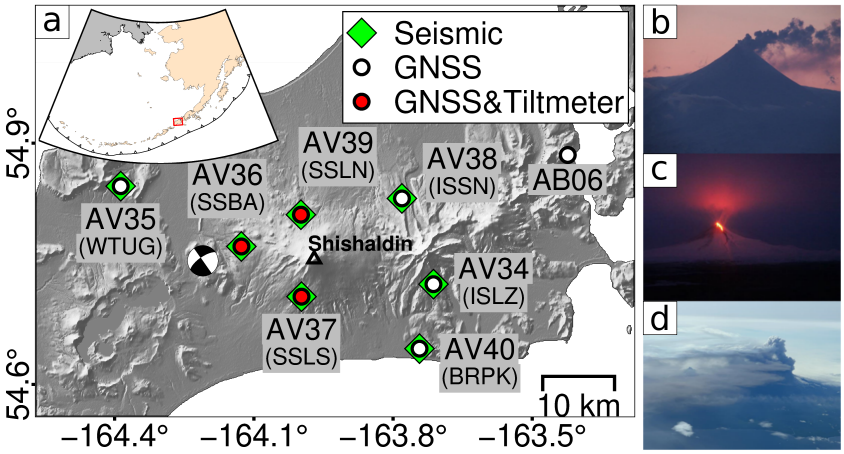

Fig. 1: Location and eruptions of Shishaldin Volcano. (a) GNSS (circles) and seismic stations (diamonds, names in parentheses) at Shishaldin; red circles represent stations with co-located tiltmeters, the beachball represents the focal mechanism for the M_L 5.2 earthquake on March 4, 1999 (Moran et al., 2002). The inset shows the location of the main map area (red rectangle) in the context of Alaska's Aleutian Arc; the black line with triangles shows the convergent plate boundary. (b) Summit degassing on May 7, 2015. Photo courtesy of Allan and Kathy Lowe (AVO database ID: 78791). (c) Lava flow on late December, 2019. Photo courtesy of AVO (AVO database ID: 159861). (d) Ash plume on August 4, 2023. Photo courtesy of Chris Barnes (AVO database ID: 194630).

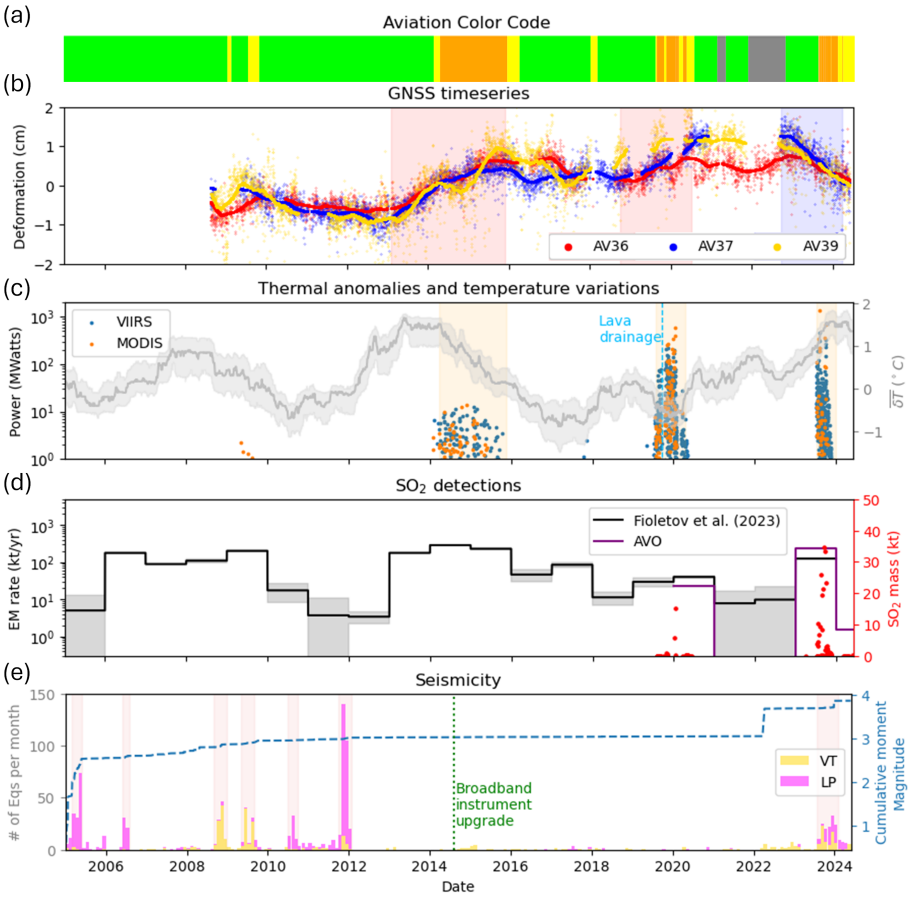

Fig. 2: Aviation Color Code and multidisciplinary data between January 1, 2005 and June 1, 2024. (a) Aviation Color Code given by AVO. (b) GNSS radial deformation time series for the three stations at Shishaldin's edifice, red and blue backgrounds represent inflation and deflation periods respectively. (c) Radiative power for the thermal anomalies detected with HotLINK using MODIS (orange points) and VIIRS (blue points) imagery. The gray line represents the low-temperature diffuse thermal anomalies in the flanks of the edifice and the gray zone the uncertainty, the reference temperature ($\overline{\delta T} = 0°C$) is set on January 1, 2005. The orange backgrounds represent the eruption spans and the cyan dashed line the lava drainage event on September 19, 2019. (d) SO_2 emission rate from AVO (Loewen, This issue; Lopez et al., This issue). The purple line is the annual emission rate (kt/yr) and the red points the daily SO_2 mass. The black line is the SO_2 emission rate from the Fioletov et al. (2023) catalog and the gray zone is the uncertainty. (e) Earthquake rate per month and cumulative moment magnitude. Magenta color represents the portion of LP events and gold represents the portion of VT events. The pink backgrounds represent the time spans of the seismic swarms and the green dotted line the upgrade of the network with broadband instruments on August 7, 2014.

4.1 Thermal and Gas Remote Sensing

4.1.1 Thermal anomalies

We use thermal remote sensing data from the Moderate Resolution Imaging Spectroradiometer (MODIS) and the Visible Infrared Imaging Radiometer Suite (VIIRS) sensors. To detect and quantify volcanic thermal anomalies in these data, we apply the Hotspot Learning and Identification NetworK (HotLINK) (Saunders-Shultz, Lopez, Dietterich, & Girona, 2024), a machine learning model that implements a Convolutional Neural Network architecture. HotLINK has been trained to detect volcanic thermal anomalies using the mid-infrared (3–5 μm) and thermal-infrared (5–20 μm) wavelengths. The algorithm takes as input 64×64 pixel images, and outputs a pixel's probability to represent a volcanic thermal anomaly for a 24×24 pixel area around the vent. For each thermal anomaly, HotLINK calculates the combined radiative power. Because daytime detections are more likely to be false positives, we remove these, and we further only use high confidence thermal anomalies - with a HotLINK-predicted probability > 0.9.

The radiative power of the recent eruptions reached 10 MW during the 2014–15 eruption, and approached 1000 MW and up to 1400 MW during the 2019–20 and 2023 eruptions, respectively (Figure 2c). HotLINK detects thermal anomalies during the periods of volcanic unrest and periods where the ACC/VAL was ORANGE/WATCH or RED/WARNING (i.e., 2014–15, 2019–20 and 2023). The anomalies for the 2019–20 eruption show a gap in September 2019 related to the lava drainage event described in the volcanic chronology (cyan dashed line in Figure 2c) (Orr et al., 2023). The spatial cumulative distribution of HotLINK-hotspot detections for a location shows that the high-temperature thermal anomalies are mostly confined to the summit (Figure 3). Only some detections are located outside the vent, perhaps associated with lava and pyroclastic flows from the 2019–20 and 2023 eruptions.

We can use the radiative power measurements (Figure 2c and the magma composition from Stelling et al., 2002) to estimate effusively-erupted lava volumes. According to the empirical relation for effusive eruptions from Coppola, Laiolo, Piscopo, and Cigolini (2013),

$$\mathrm{Vol} = \frac{\mathrm{VRE}}{\mathrm{c_{rad}}} \tag{1}$$

where Vol is the erupted lava volume, VRE is the volcanic radiative energy and $\mathrm{c_{rad}}$ is the radiant density that depends on the silica content. Tephra samples from the 1999 eruption show that the composition of silica in the magma is ~ 50 wt% (Stelling et al., 2002). Because this method has been developed for effusive eruptions, it is applicable to the activity during the effusive periods of the 2014–15 eruption and the early phase of the 2019–20 eruption. We calculate cumulative radiative energy releases of $\sim 1 \times 10^{14}$J and $\sim 3 \times 10^{14}$J for the 2014–15 and 2019–20 eruptions, respectively.

With this, we estimate 0.7 Mm^3 and 3 Mm^3 volumes of extruded lava for the 2014–15 and 2019–20 eruptions, respectively (Figure S1).

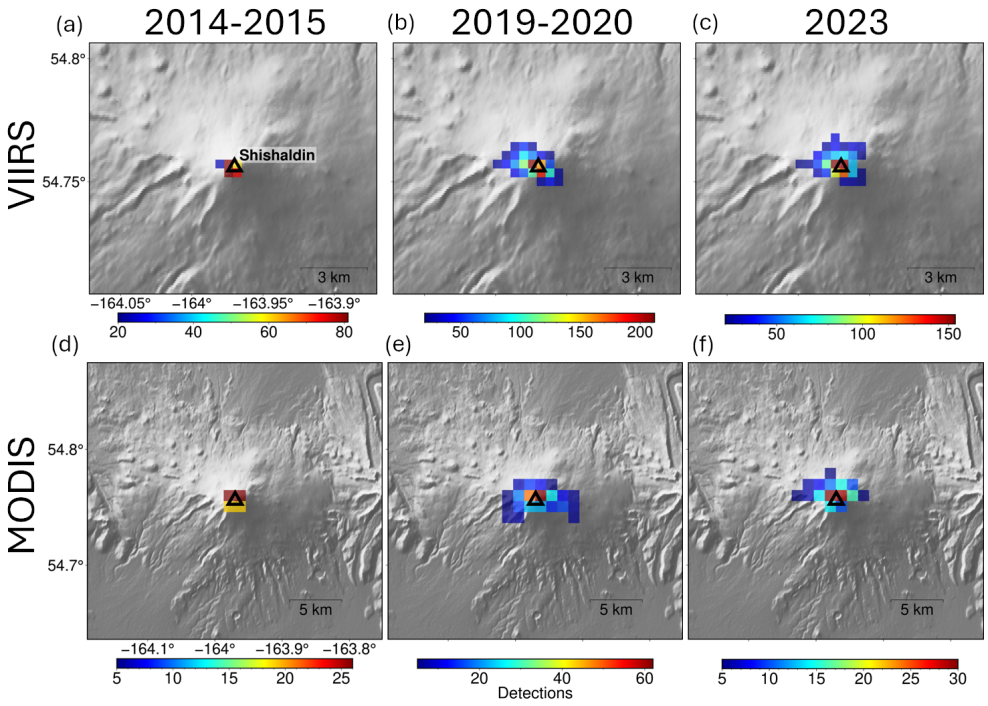

Fig. 3: Spatial histogram of thermal detections over three recent eruptions. (a-c) VIIRS detections for the 2014–15, 2019–20, and 2023 eruptions, respectively; (d-f) MODIS detections for the 2014–15, 2019–2020, and 2023 eruptions, respectively. We apply a threshold of $\geq$ 5 detections for MODIS and $\geq$ 20 detections for VIIRS to avoid plotting occasional and false positive detections.

To track subtle changes in heat emissions, we quantify diffuse, low-temperature thermal anomalies ($\overline{\delta T}$) over Shishaldin's upper edifice (a 16 km^2 square area centered on the summit) relative to a surrounding non-volcanic reference region, using MODIS thermal infrared data and following the approach of Girona and Brenot (2026) and Girona, Realmuto, and Lundgren (2021). This analysis shows that diffuse thermal anomalies increased 1 °C between 2006 and 2008, prior to the 2009 volcanic unrests (Figure 2a,c). Then it decayed to background levels in mid-2010. The anomaly then increased to $\sim$2 °C by 2013 and decayed following the onset of the 2014-2015 eruption, returning to background levels by 2017. A renewed increase is observed in 2018, which subsided in 2019 and subsequently peaked in late 2021 ($\sim$1 °C), followed by a modest decrease in mid-to-late 2022. The anomaly reached its highest value ($\sim$2 °C) toward the end of the 2023 eruption and began to decay after the eruption concluded.

4.1.2 Volcanic Gas Emissions

We use annual average SO_2 emission rates from 2000-2022 provided by the Fioletov et al. (2023) catalog from the TROPOspheric Monitoring Instrument (TROPOMI), the Ozone Mapping and Profiler Suite (OMPS) and the Ozone Monitoring Instrument (OMI) satellite sensors to track long-term trends in volcanic degassing. We complement this dataset using individual SO_2 detections and masses that AVO calculated from TROPOMI data (Loewen, This issue; Lopez et al., This issue) from 2019–2024. In order to compare average annual emission rates and individual SO_2 masses, we sum the SO_2 masses in the AVO catalog for each available year. More details of the methods used to calculate SO_2 masses can be found in Fioletov et al. (2023) and Lopez et al. (This issue).

The annual average emission rates reported by Fioletov et al. (2023) between 2013 and 2016 reached 287 kt/yr, higher than the rates between 2019 and 2020 (30–40 kt/yr) and during 2023 (125 kt/yr) (Figure 2d). AVO detections report larger cumulative SO_2 masses for the 2023 eruption (236 kt) than the 2019–20 eruption (24 kt) (Loewen, This issue). However, the 2019–20 eruption occurred in winter, when the detection capabilities of ultraviolet satellite sensors used in this study are limited at high latitudes (e.g., Lopez et al., 2013). Lopez et al. (This issue) compare their 2019–2020 cumulative SO_2 eruption mass with that calculated from the Infrared Atmospheric Sounding Interferometer (IASI) sensor for the same time period, and estimate that TROPOMI may have underestimated the 2019-2020 SO_2 eruptive mass by 25%. With total emissions of 236 kt, the 2023 annual SO_2 emission mass is substantially higher than 2019-20 and similar to total emissions between 2013-2016. The discrepancies between the Fioletov et al. (2023) and AVO catalogs may be due to differences in data sources (i.e., TROPOMI for AVO and TROPOMI, OMPS and OMI for Fioletov et al., 2023) and measurement techniques (Lopez et al., This issue). The Fioletov et al. (2023) method uses a pixel averaging and wind rotation method around an identified source to calculate emission rates, while in the AVO method an analyst identifies each plume and links it with a volcanic based on modeled backward wind trajectories. Discrepancies could occur between these two methods for detached Shishaldin clouds that may not be located near the source or in cases when SO_2 from nearby volcanoes could be misattributed to Shishaldin using automated techniques.

4.2 Seismicity

We use the AVO earthquake catalog to calculate the b-value for the entire catalog of events within a 15 km radius from Shishaldin's vent. We filter out events that fall below the magnitude of completeness of $M_c = 0.6$ (Figure S2), determine monthly earthquake counts, and track the spatiotemporal evolution of hypocenter locations for prominent seismic swarms that occurred since the installation of the seismic network.

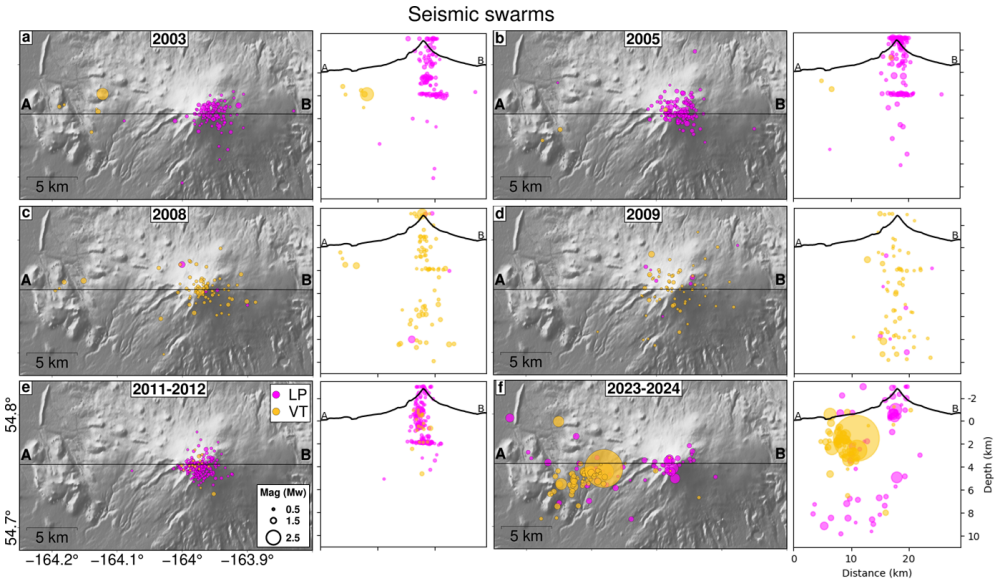

Fig. 4: Seismic swarms since the 1999 eruption between -3–10 km bsl depth. Seismic swarms between: (a) July 1, 2003 and November 1, 2003, (b) March 1, 2005 and June 1, 2005, (c) September 1, 2008 and December 31, 2008, (d) May 1, 2009 and September 1, 2009, (e) November 1, 2011 and January 29, 2012, (f) July 28, 2023 and February 1, 2024. Left, top-down view of the hypocenters. Right, longitude-depth plots of the hypocenters projected onto the AB profile (black line) in the left panels. Note that earthquakes that locate above the ground surface are typically artifacts of earthquake location uncertainty, arising from limitations in the seismic velocity model, data quality, or station coverage, rather than actual seismic events occurring in the air.

The AVO earthquake catalog demonstrates that Shishaldin exhibited minimal discrete seismic activity between 2013 and 2022, despite the 2014–15 and 2019–20 eruptions (Figure 2e, S3). However, before this long period of low seismic activity, Shishaldin produced several pronounced seismic swarms following the 1999 eruption and during the 2009–2012 time period (Figure 2e). Most of the seismicity documented then was of volcanic origin, considering that it concentrated below the shallow edifice near Shishaldin's vent (Figures 4, and S4). The seismic swarms at Shishaldin are primarily composed of VTs or LPs instead of a mix of both within individual swarms (Figure 2e). These swarms occur in an intermittent pattern through time and have occupied the same seismogenic area directly underneath the summit (Figure 4), indicating that this source region can host multiple styles of seismic activity. While the VT earthquakes appear more distributed throughout Shishaldin's edifice, the hypocenters of the LP earthquakes from 2000–2012 are mostly constrained within depths of < 2 km bsl. This depth distribution of LPs is likely associated with the shallow and seismically active portion of Shishaldin's conduit, which hosts the degassing-related LP source mechanisms proposed in earlier work (Caplan-Auerbach & McNutt, 2003;

Caplan-Auerbach & Petersen, 2005; Petersen, 2007; Petersen et al., 2005; Petersen & McNutt, 2006).

The 2023 eruption, although primarily characterized by seismic tremor and weak LP events like the preceding eruptions (Fee et al., This issue), also exhibited a small VT seismic swarm from mid-August 2023 (one month after the eruption started) to January 2024 (two months after the eruption ended) (Figure 2e). This VT swarm was spatially separated from the LPs sequence; while the LPs located shallowly around Shishaldin's edifice, the VTs clustered in a location 12 km southwest of the summit (Figure 4f). Previously, an energetic M_L 3.6 event occurred in this zone on April 10, 2022 (Figure 2e, see kink in cumulative moment magnitude curve). Notably, the VT cluster was located in the proximity of the mainshock-aftershock sequence of the M_L 5.2 earthquake from March 4, 1999, suggesting a possible tectonic component.

To understand the nature of Shishaldin's seismicity in more detail, we apply the VOlcano Infrasound and Seismic Spectrogram Neural Network (VOISS-Net) (Fee et al., 2025; Tan et al., 2024) to data from the three closest seismic stations between 2004 to 2024. VOISS-Net classifies the seismicity into seven categories: broadband tremor, harmonic tremor, monochromatic tremor, volcano-tectonic earthquakes, long-period earthquakes, explosions, and noise. To ensure the reliability of the VOISS-Net results, we retain only classifications for which the network-averaged probability (the mean of per-station class probabilities) exceeds 0.4. As demonstrated by Fee et al. (2025), this threshold choice balances classification confidence and classification retention across numerous examples.

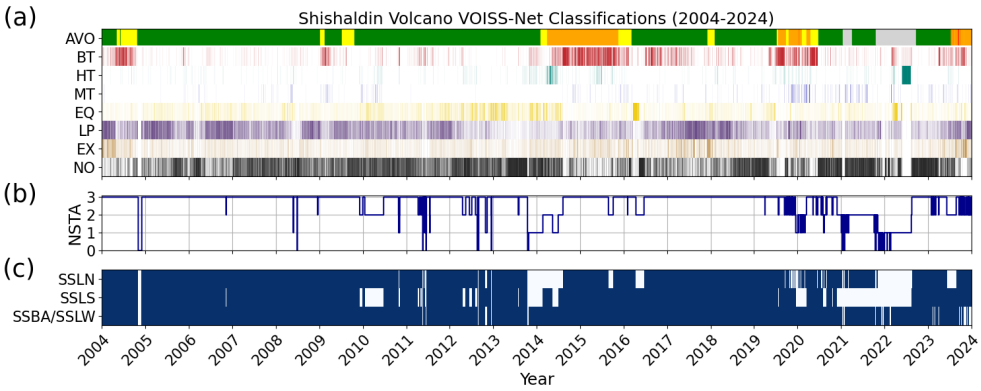

Fig. 5: VOISS-Net results from 2004 to 2024 for the stations SSLW/SSBA, SSLS and SSLN (collocated with AV36, AV37 and AV39 respectively). (a) Aviation Color Code (AVO) and classification of seismic signals into broadband tremor (BT), harmonic tremor (HT), monochromatic tremor (MT), volcano-tectonic earthquake (EQ), long-period (LP), explosions (EX) and noise (NO). (b) Number of stations available. (c) Outages in the stations (blue operational, white not-operational). Note that stations SSLW and SSBA ran alongside one another on the same ridge west of Shishaldin from mid-2008 to mid-2019. When SSBA data is available for VOISS-Net classification, we discard SSLW's contribution to prevent a bias. Note that VOISS-Net classifications, although filtered by probability, may still include occasional misclassifications related to station availability and local noise conditions.

Over the 20-year period of VOISS-Net analysis, tremor signals largely coincided with observed volcanic activity and changes in ACC/VAL by AVO (Figure 5). Most tremor observations at Shishaldin are classified as broadband tremor, which are long-duration signals with a broad (> 1 Hz) frequency peak below 5 Hz (Tan et al., 2024). We observe a possible increase in VT signals prior to the 2014–15 eruption, although this period contains very few events in the AVO catalog (Figure 2e), likely due to noisy conditions and station outages (Figure 5b,c). This observation was followed by a rise in LP signals until 2018, when the LP rate declined until the onset of the 2019–20 eruption. We also observe intermittent VT and LP signals in the VOISS-Net classification over the entire analysis period (Figure 5), which is broadly consistent with the VT and LP seismic rates documented in the AVO catalog (Figure 2e).

4.3 Geodesy

To reassess the nature of deformation at Shishaldin, we reanalyze continuous GNSS and tilt data from its ground-based geodetic network (Figure 1). Installed in 2007 as part of the EarthScope[1] Plate Boundary Observatory network, the Shishaldin geodetic network consists of six continuous GNSS stations and three collocated borehole tiltmeters at the edifice stations AV36, AV37 and AV39 (Freymueller & West, 2024).

[1] Formerly UNAVCO

The GNSS stations have remained mostly operational since their installation with occasional outages (Figure S5).

To model deformation in the context of subsurface pressure sources, we run Bayesian inversions using analytical models implemented in the Versatile Modeling of Deformation (VMOD) inversion framework (Angarita, Grapenthin, Henderson, Christoffersen, & Anderson, 2024). We test several different deformation source geometries such as a finite sphere (McTigue, 1987), a spheroid (Yang, Davis, & Dieterich, 1988), an open conduit (Nishimura, 2009), and a dike (Okada, 1985). These models do not account for topography, which may introduce biases in the modeled deformation and propagate into the inferred source parameters (e.g., Figure 6 in Crozier et al., 2023). The number of steps in the inversions depends on the amount of model parameters. For instance, for the spherical geometry (the model with the least number of parameters) the inversion has 1 million steps and for the dike geometry (the model with the most parameters) the inversion has 5 million steps. In all cases the inversions discard the first 100 thousand samples to eliminate biases on the initial parameter value choices (burn-in), and to eliminate autocorrelation, we sub-sample at every 1000th step to determine the posterior distributions (e.g., Angarita et al., 2024; Aster, Borchers, & Thurber, 2018).

4.3.1 GNSS

We estimate daily GNSS positions in the 2014 International Reference Frame (ITRF14, Altamimi, Rebischung, Métivier, & Collilieux, 2016), using NASA's Jet Propulsion Laboratory's (JPL) orbit, clock and ionospheric correction products, and the International GNSS Service (IGS) antenna phase center models (Dow, Neilan, & Rizos, 2009) in an automated JPL GipsyX-based Bertiger et al. (2020) workflow described in Grapenthin, Kyle, et al. (2022). Tectonic motion, such as long-term plate motion and interseismic strain build-up due to plate coupling and earthquake offsets (e.g., Xiao et al., 2021), is removed by referencing the stations to nearby AV35 (Figure S5). To detect deformation episodes, we evaluate radial deformation by rotating the horizontal components into the radial and transverse directions of the station relative to the vent location (54.756, -163.97). To eliminate noise in the daily time series, we apply a 100-day window moving average filter. For individual deformation episodes, we compute long-term velocities using the Create and Analyze Time Series (CATS) software (Williams, 2008) applying a white noise model.

We resolve pre-eruptive inflation for the 2014–15 eruption and the 2019–20 eruptions, and pre- and syn-eruptive deflation for the 2023 eruption (Figure 2b). It appears that pre-eruptive inflation was absent for the last eruptive period, although this may be due to data gaps at AV37 and AV39. The long-term radial velocities for the first inflation episode (average > 5 mm/yr) are larger than those during the second inflation episode (average < 5 mm/yr). The long-term velocities during the deflation period are similar in magnitude to the first inflation episode (> 5 mm/yr). The cumulative radial deformations are small: ~ 1.5 cm and ~ 1 cm for the first and second inflation episodes, respectively, and $\sim$-1 cm for the deflation episode (Figure 6a–c).

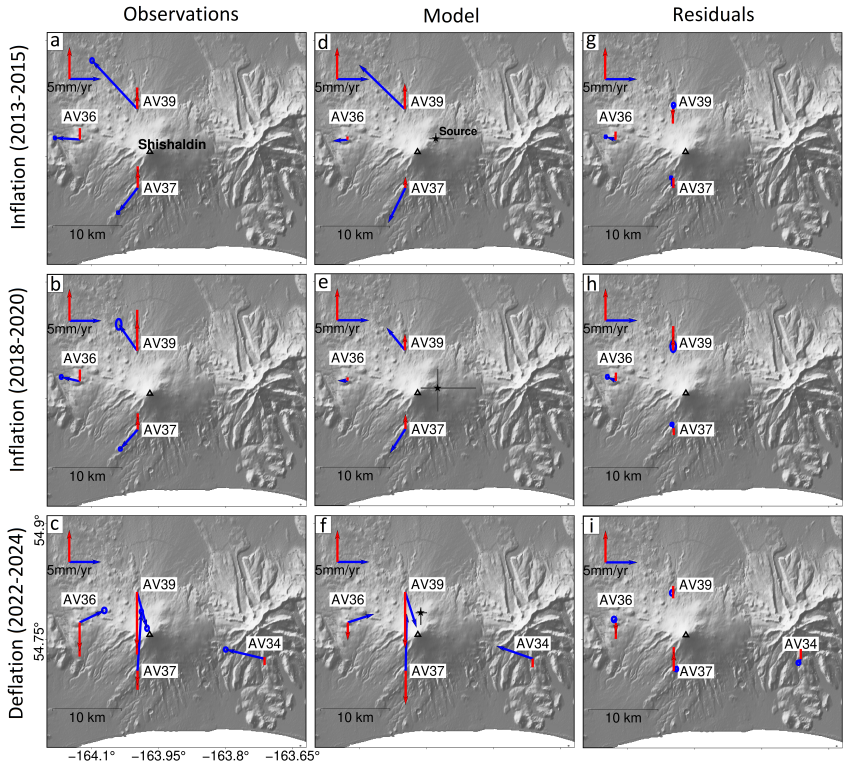

Fig. 6: GNSS velocities for the inflation episodes (a) from February, 2013 to November, 2015, and (b) from October, 2018 to June, 2020 and (c) the deflation episode between September, 2022 and April, 2024. Modeled deformation from the maximum a posteriori (MAP) solutions using (d,e) a spherical source and (f) a spheroidal source. (g,h,i) Respective model residuals. Blue and red arrows represent horizontal and vertical velocities, respectively, blue circles and red lines are the uncertainties for the horizontal and vertical components, respectively, stars are the MAP solutions for source locations and the black lines are the source location uncertainties.

Inverting data from the deformation episodes suggests that spherical pressurized source persisted for the 2014–15 and 2019–20 eruptions below Shishaldin's edifice at $\sim$2–4 km bsl depth (Table 1, Figures 6d,e,g,h, S6, S7). The conduit model fits similarly well, but requires more parameters (Table S1), and the resulting radius/length ratio of the conduit ($\sim$3–9) is unrealistic (Figures S8, S9). The dislocation model also fits the data reasonably well, but the limited number of observations and the larger number of parameters required by the Okada (1985) model lead us to favor the spherical source (Table S2). Moreover, the spherical-source inversions yield consistent depths for both inflation episodes, unlike the dislocation-source results (Figures S10, S11). The deflation is explained by a spheroidal source, which reproduces the deformation

at the stations AV36, AV37, AV39, and AV34 (Figures 6f, and i). The posterior distributions in this case suggest a vertical spheroid (possible conduit) (Table 1, Figure S12). The deflation can also be explained by two spherical sources. To reduce the number of inversion parameters, we decide to fix the location, depth and radius for one of the sources according to the inversion results of the inflation episodes (Figure S13). Although the deformation pattern is well-explained (Table S1), the deep source is $\sim$9 km northwest from the vent (Figure S14) which seems unlikely, though we note a small cluster of five seismic events at 6–13 km depth and $\sim$9–10 km NW from the vent. Laterally offset magma reservoirs $>$9 km from the edifice have been identified at other arc volcanoes (Lerner et al., 2020; Lundgren, Samsonov, López Velez, & Ordoñez, 2015). The modeled spheroidal source, however, is offset less than 2 km from the vent. Additionally, the increase in the number of parameters is not statistically justifiable. For these reasons, we prefer the spheroidal geometry to explain the deflation episode, but acknowledge the alternative model.

Table 1: Parameters for the maximum a posteriori models and uncertainties (from the 95% confidence intervals) for the deformation episodes in the GNSS network

Parameter	Sphere (Inflation 2013–15)	Sphere (Inflation 2018–20)	Spheroid (Deflation 2022–24)
Longitude (°)	$-163.929^{+0.041}_{-0.015}$	$-163.925^{+0.086}_{-0.038}$	$-163.964^{+0.014}_{-0.011}$
Latitude (°)	$54.773^{+0.007}_{-0.006}$	$54.739^{+0.085}_{-0.059}$	$54.784^{+0.007}_{-0.016}$
Depth (km − bsl)	$1.92^{+2.30}_{-1.18}$	$3.40^{+4.52}_{-2.49}$	$6.34^{+2.05}_{-1.01}$
Radius/ Semimajor (km)	$0.51^{+0.69}_{-0.16}$	$0.67^{+0.29}_{-0.16}$	$5.24^{+2.74}_{-3.411}$
Semiminor (km)	-	-	$0.26^{+0.48}_{-0.15}$
Pressure (mμ/yr)	$5.04^{+5.41}_{-3.46}$	$1.64^{+3.01}_{-2.98}$	$-4.28^{+3.22}_{-5.53}$
Azimuth (°)	-	-	103^{+182}_{-58}
Dip (°)	-	-	75^{+9}_{-16}
ΔVolume (Mm^3/yr)	$2.32^{+1.52}_{-0.65}$	$1.93^{+0.72}_{-0.77}$	$-8.46^{+2.15}_{-2.82}$

4.3.2 SAR & InSAR

In addition to the ground-based geodetic observations, we use a range of SAR data to assess surface deformation. We process interferometric pairs from the European Remote Sensing (ERS-1/2), Advanced Land Observing Satellite (ALOS-1), and Sentinel-1 SAR satellite missions. For the ERS-1/2 processing we use GMTSAR (Sandwell, Mellors, Tong, Wei, & Wessel, 2011), for ALOS-1 imagery we use the

InSAR Scientific Computing Environment (ISCE-2) (Rosen, Gurrola, Sacco, & Zebker, 2012), and for Sentinel-1 we use the Alaska Satellite Facility's workflows (Grapenthin, Cheng, et al., 2022; Hogenson et al., 2016). We choose interferograms with high coherence values to generate time series with the Miami InSAR time-series software in Python (MintPy) (Yunjun, Fattahi, & Amelung, 2019) as detailed in Grapenthin, Cheng, et al. (2022). We also use the amplitude of TerraSAR-X images during the 2023 eruption to infer elevation changes utilizing the Morphology from SAR toolbox (MoSARt) algorithm described by Angarita, Grapenthin, Plank, Meyer, and Dietterich (2022).

The resulting InSAR velocities (Figure S15) do not reveal any significant deformation (less than 3 cm for Sentinel-1 between 2014–24 and less than 10 cm for ALOS-1 between 2007–11). This is consistent with the low deformation rate observed in the GNSS time series (Figure 2b). The extent of the decorrelated area is similar to the one found by Moran et al. (2006) and Lu and Dzurisin (2014).

We infer elevation changes from TerraSAR-X amplitude imagery for the 2023 eruption similar to Angarita et al. (2022) (Figure S16). The results show elevation increases ($\sim$20 m) on August 9, 2023 likely related to tephra and pyroclastic deposits filling in the summit crater during a paroxysm on August 4, 2023. Then, we observe elevation decreases ($\sim$50 m) on September 9, 2023 related to the appearance of a crack from the crater towards the NE flank. The seismic network and photographs taken by AVO staff documented a rim collapse that contributed to the crack formation on August 28, 2023 (Figure S17). We find additional elevation decreases ($\sim$70 m) on October 3, 2023 showing the propagation of the crack towards the SW direction.

4.3.3 Tilt

The tilt observations come from self-leveling tiltmeters installed in 4–6 m deep boreholes. AVO re-leveled them in 2014 and 2016 when they had drifted off level and saturated. The sampling rate was increased from 1 sample per minute to 1 sample per second during the 2019–20 eruption for higher temporal resolution deformation recording. We derive long-term daily time series and apply thermal and instrumental drift corrections (Battista, Pavoni, & Vanali, 2024; Furst, Chéry, Mohammadi, & Peyret, 2019) (Figure S18). We assume that tilt measurements can be expressed as:

$$a_m(t) = a_s(t) + a_T * T(t) + a_D * t \tag{2}$$

where t is time, $a_m(t)$ is the measured tilt signal, $a_s(t)$ is the actual surface inclination, a_T is temperature coefficient of the sensor thermal drift, T(t) is the sensor's temperature, and a_D is the instrumental drift coefficient. The instrumental drift on borehole-tiltmeters is difficult to determine because of the absence of a reference or absolute measurement system (Furst et al., 2019). Tilt observations for geophysical applications reported linear drift over several months of recordings (Goulty, 1976; Sakata & Sato, 1986), attributed to changes in the surrounding rock and mounting instabilities (Sakata & Sato, 1986). Since snow coverage at the base of the Shishaldin edifice (where the tiltmeters are located) varies significantly between summer and

winter (Robinson & Estilow, 2012), we perform separate corrections for each season. We rotate the tilt time series into the radial and transverse directions relative to Shishaldin's vent and the station location to identify deformation episodes.

Despite thermal and drift corrections, the noise prior to the 2014–15 eruption is significant (Figure S18). For the 2019–20 eruption, the tiltmeters captured a lava drainage event on September 19, 2019 (Figures 7a, and S19) preceded by an outward tilt three months before (Figure S20). For the 2023 eruption, the tiltmeters incline towards the vent during explosions on October 3, and November 2, 2023 (Figures 7b,c, and S19). We run inversions for tilt observations produced by these events using the steady state solution from Nishimura (2009) for an open conduit (Table 2, Figure S21). Given the limited observations for each event (two and three stations), we fix the horizontal location of the conduit at Shishaldin's vent and reduce the number of inversion parameters by estimating a single set of geometric parameters (i.e., radius, length, depth) and individual pressure changes for each event.

Table 2: Parameters for the maximum a posteriori model using the open conduit and the deformation episodes in the tilt network. LD refers to the 2019 lava drainage, Ex1 and Ex2 refer to the paroxysms on October 3 and November 2, 2023, respectively.

Parameter	Value
Depth (km − bsl)	$0.0^{+0.2}_{-0.1}$
Length (km)	$1.2^{+0.3}_{-0.1}$
Radius (m)	157^{+132}_{-32}
$\text{Pressure}_{\text{LD}}$ (MPa)	-641^{+504}_{-330}
$\text{Pressure}_{\text{Ex1}}$ (MPa)	-81^{+63}_{-45}
$\text{Pressure}_{\text{Ex2}}$ (MPa)	-93^{+73}_{-51}

Table 3: Root mean square error (RMSE) for the inversions of the tiltmeter records using the open conduit and dike models

Model	RMSE (μrad)
Open conduit	0.17
Dike	0.19

The surficial manifestation of a crack in the NE-SW direction suggests a dike geometry for magma transport (Mastin & Pollard, 1988). We compare this alternative source geometry against the open conduit for the tilt observations during the last two paroxysms of the 2023 eruption. We use the elevation decreases obtained from the SAR amplitude images to constrain some of the parameters in the inversion. We estimate

that the crack is ∼1 km long centered in the vent and has an azimuth of ∼65° (Figure S16). We use a tensile dislocation (dike) (Okada, 1985) and solve for the centroid depth, width and openings for each event (Figure S22). Based on the observations during the paroxysms, we find higher residuals for the dike geometry (Table 3 and Figure S23).

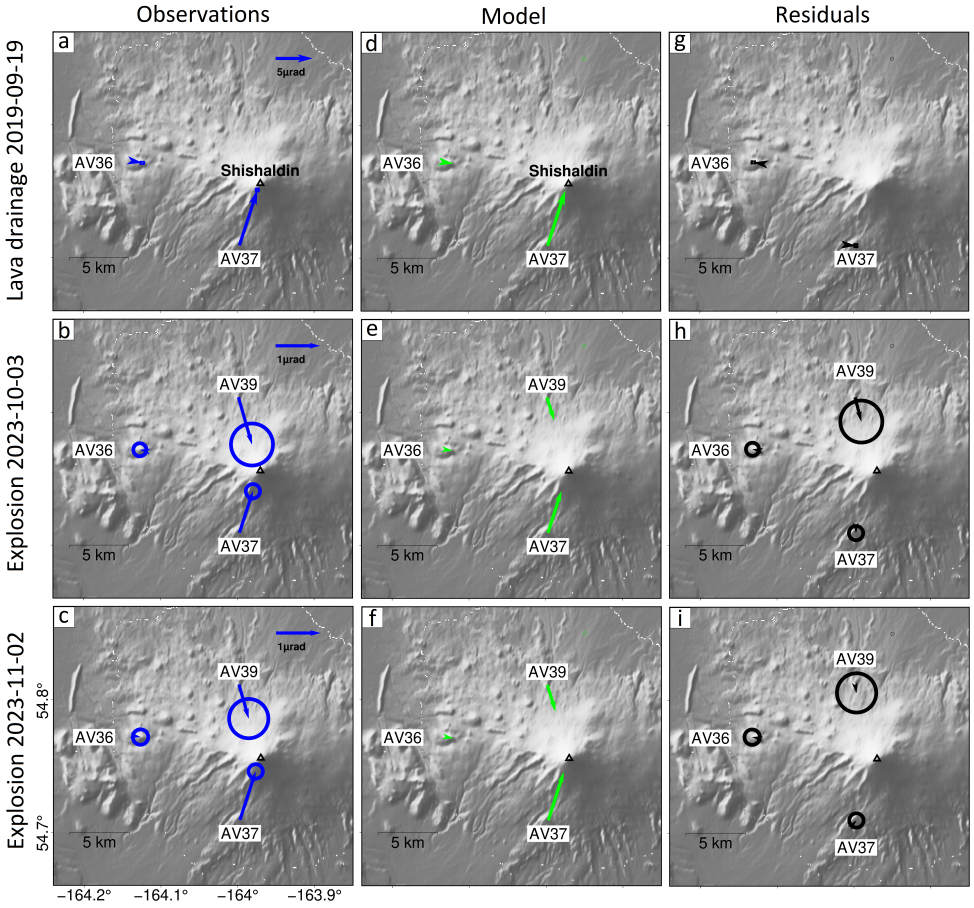

Fig. 7: Tilt observations during the (a) lava drainage on September 19, 2019 and paroxysms on (b) October 3 and (c) November 2, 2023. (d,e,f) Modeled tilt for the maximum a posteriori solution using the open conduit model. (g,h,i) Model residuals.

Inflation preceding volcanic explosions has been observed in tiltmeter records at other volcanoes (Christoffersen et al., 2025; Genco & Ripepe, 2010; Lyons, Waite, Ichihara, & Lees, 2012). Although the lava drainage event did not result in an explosion, the tilt inflation signal detected three months prior the event is likely related to magma ascent processes in the open conduit (Nishimura, 2009). We explore possible magma

degassing processes that could explain the tilt motion observed prior to, and that ultimately caused, the 2019 lava drainage event. We assume that before the lava drainage event the conduit magma contained a high proportion of exsolved gas relative to melt and occupied a relatively large volume. Then, upon release of the exsolved gas, the remaining melt was much less voluminous and was no longer able to fill the conduit. We run forward time-dependent models where the strength of the pressure source is modulated by three different magma degassing regimes (Nishimura, 2009). In the first model the bubbles in the magma do not grow in size and rise with the melt. In the second model, the bubbles increase in size as a result of diffusion mass transfer from water molecules as they rise with the melt. In the third model, the bubbles grow in size because they rise faster than the melt, reducing the pressure surrounding the bubbles (Figure S20). The second model where bubble size increases due to diffusion mass transfer from water molecules, while magma rises with the melt offers the best fit with the time series.

4.3.4 Interaction of deformation sources with tectonic and geomorphological features

The seismicity observed during the 2014–15, 2019–20, and 2023 eruptions shows distinct trends compared to the previous decade as discussed in earlier sections. Because the models that explain the observed inflation and deflation (McTigue, 1987; Yang et al., 1988) also solve for the internal deformation within the half-space isotropic medium, we can evaluate the potential effects of the corresponding deformation events in triggering the observed tectonic seismicity. We calculate the strain field from finite differences of the forward-modeled deformation field and estimate the stress change from this strain field, assuming a Young modulus of 80 GPa, a value typically used for Coulomb stress changes (King, Stein, & Lin, 1994). The shear and normal stresses acting on a plane within a stress field, and therefore the Coulomb stress changes, depend on the orientation of the plane. To constrain this, we use the focal mechanism for the M_L 5.2 event in March 1999 as deduced by Moran et al. (2002). They indicated the earthquake occurred by strike-slip faulting along a SE- or SW-oriented vertical fault plane with strike/dip 145°/90° or 235°/70°, respectively (Figure 1a). The interferograms from Moran et al. (2006) suggest the former orientation for the fault plane. Thus, we calculate the Coulomb stress changes caused by each source on a left-lateral strike-slip receiver faults with strike/dip of 145°/90°.

We calculate the Coulomb stress change rates for each source using the parameters in Table 1. These rates were then multiplied by the number of years each source was deforming to calculate the cumulative Coulomb stress changes since February, 2013 (onset of the first inflation episode). The results reveal that most earthquake hypocenters lie within regions of Coulomb stress increase (Figures 8a,b). The largest magnitude events occurred in a zone of continuous Coulomb stress increase (Figures 8a,b, and S24). Thus, pressure changes in the magmatic system could have incrementally pushed the host fault to failure due to repeated static loading.

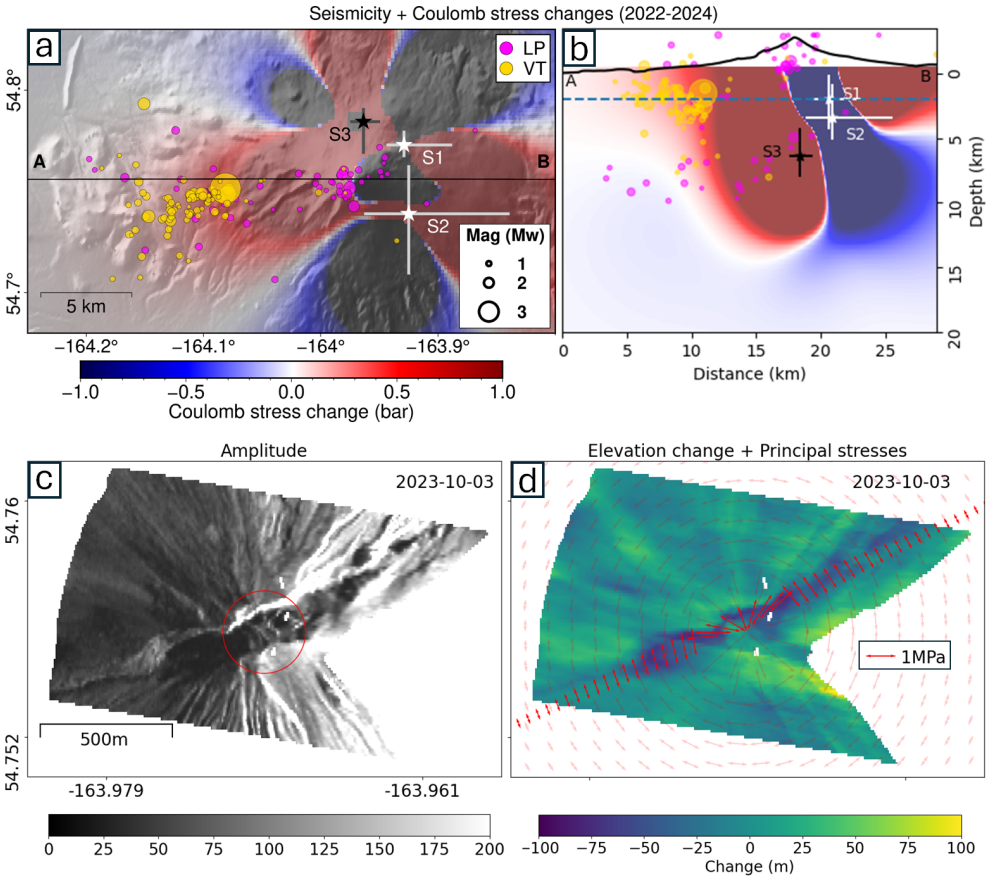

Fig. 8: Interaction of deformation source with tectonic and geomorphological features. (a) Cumulative Coulomb stress changes at 2 km bsl depth caused by the deformation sources in Table 1 and seismicity during the deflation period (from September, 2022 to February, 2024). (b) Cross-section along black line in (a), the dotted line represents the 2 km depth shown in (a). White stars represent inflation sources and the white line represent the uncertainties in the location, the black star represents the deflation source and the black lines the uncertainty in the location. (c) TerraSAR-X amplitude image at October 3, 2023. The red circle shows the size of the conduit according to Table 2. (d) Derived elevation changes (from July, 29 and October 3, 2023) with principal stresses (σ_2) in the surface caused by an open conduit using the parameters in Table 2 . Outward red arrows reflect tensile stresses.

The mechanism causing the NE-SW crack remains unclear, as the tilt inversions in the previous subsection indicate that an open conduit is the most probable deformation source, rather than a dike geometry. These models assume a flat surface at the mean elevation of the tiltmeters ($\sim$600 m). In order to identify the stress conditions under which a crack could form, we quantify the direction and magnitude of the principal

stresses at this flat surface for an open conduit assuming that this stress state would be similar at the shallower portions of the summit. Unfortunately, the Nishimura (2009) model does not offer a solution for internal deformation. Therefore, we calculate stresses only at the surface using the geometry obtained from the inversion (Table 2, Figure 8c,d) and an overpressure of 100 MPa. The tensile stresses are significantly larger within a radius of $\sim$ 700 m around the conduit and almost perpendicular to the crack orientation in its widest portions. This suggests that the frequent pressurization events in the open conduit during the paroxysms of the 2023 eruption contributed to the propagation of the crack in the NE-SW direction.

5 Discussion

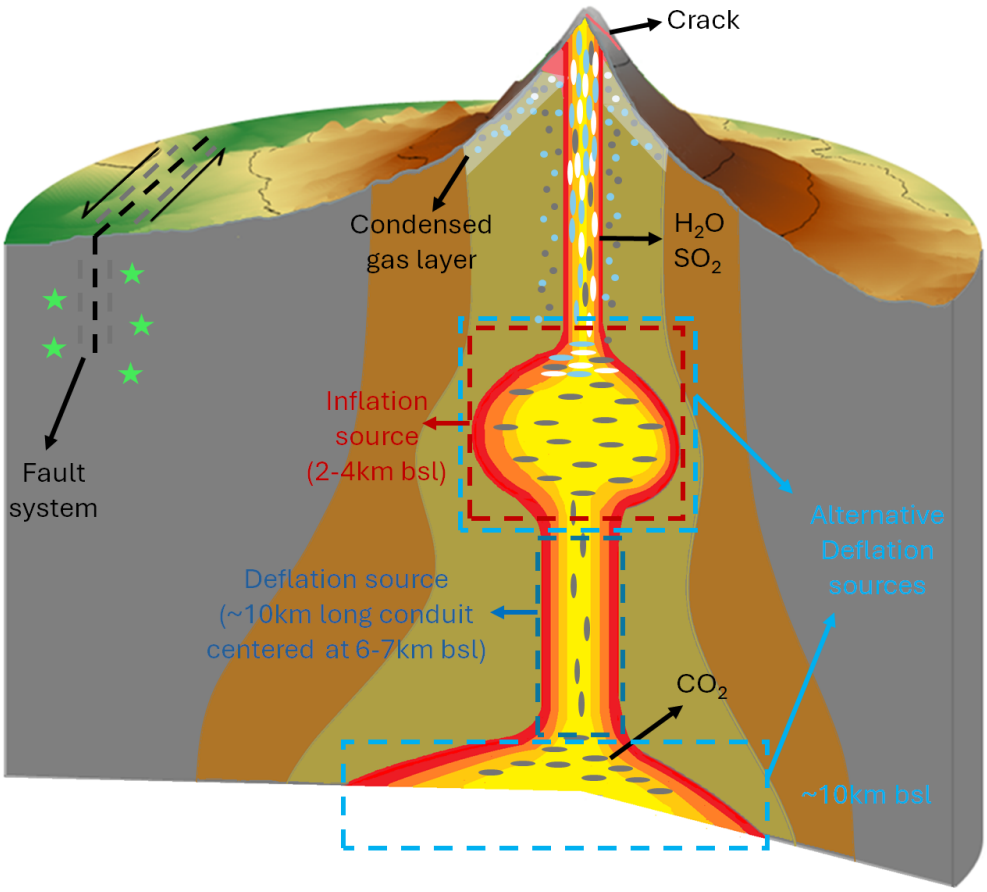

Fig. 9: Conceptual model for the magmatic system of Shishaldin Volcano. The diagram includes a shallow conduit that might have evolved into a dike in the highest portions of the edifice during the 2023 eruption, a shallow source at 2–4 km bsl depth, a long and wide ($\sim$ 500 m diameter) conduit connecting a deep magma source ($\sim$ 10 km bsl) with the shallow source. The white, gray and blue circle represent exsolved SO_2, CO_2 and H_2O gases, respectively. Condensed water vapor on the edifice flanks could contribute to a low-temperature thermal anomaly (Girona & Brenot, 2026). The dotted line represents the fault system located towards the west of the edifice, and the arrows indicate the strike-slip orientation according to Moran et al. (2002)

5.1 Magma plumbing system

Our synthesized results from different disciplines indicate that Shishaldin has a long conduit with a shallow (2–4 km bsl) magma storage region and possibly a deep magma source (∼ 10 km bsl, Figure 9). The long conduit possibly caused deflation prior to, during, and after the 2023 eruption, as suggested by the geodetic models. However, depressurization from the shallow source and a deep source (∼ 10 ± 3 km bsl) can also explain the deflation episode. Geochemistry models (Lopez et al., This issue; Rasmussen et al., 2018) based on petrologic constraints from the 1999 eruption indicate exsolution and potential degassing of CO_2 from magma likely begins at depths consistent with the deep source.

The geodetic models support the existence of the shallow source at 2–4 km bsl depth. Geochemical models indicate that exsolution and degassing of SO_2 and H_2O from the host magma may begin at the upper portion of the shallow storage region and may partially contribute to the deformation observations indicating a pressurized source, interpreted here to be associated with magma intrusions prior to and during the 2014–15 and 2019–20 eruptions. These models suggest that SO_2 and H_2O exsolve predominantly at shallower depths – within the volcanic edifice itself. Furthermore, the inferred shallow storage region lies just beneath the depth range of LP seismicity, which occurs primarily at 2 km bsl and shallower. As these LP swarms are interpreted to reflect bubble nucleation or coalescence and unsteady flow processes (Caplan-Auerbach & Petersen, 2005; Cusano et al., 2015; Petersen, 2007), they support shallow H_2O and SO_2 exsolution and their degassing pathways. The creation of this shallow source might have also enhanced SO_2 emissions during 2013, coinciding with the start of the first inflation episode (Figure 2b,d). The lack of evidence for magma mixing between remnants from the 1825 eruption and magma from the 1999 eruption (Stelling et al., 2002) indicates that shallow storage might be short-lived ($\leq$ decades), perhaps transient. Geochemical evidence from Rasmussen et al. (2018) suggests that magma recharge may occur months prior to the eruption.

We attempt to resolve the shallow sources with inversions of the tiltmeter records. Previous studies have suggested geometric constraints for the shallow deformation sources: Moran et al. (2002) proposed a dike geometry that was parallel to the direction of convergence of the Pacific and North American plates supported by the presence of cinder cones on the NW flank of the edifice. However, the proposed azimuth is not consistent with recent observations, as the final stages of the 2023 eruption produced a summit crack with a NE-SW orientation, roughly perpendicular to the subduction direction. This is consistent with observations of local stress field rotations, in cases approaching independence of the regional stress field in volcanoes due to edifice load, magma pressure, and edifice elevation (Pérez-Estay et al., 2023; Vargas-Bracamontes & Neuberg, 2012). Several studies support a conduit geometry based on seismo-acoustic observations between 2002–04 (Caplan-Auerbach & Petersen, 2005; Petersen & McNutt, 2006). In this study, the open conduit and dike geometries reproduce the observed tilt during the last two paroxysms of the 2023 eruption (Figures 7, and S13). However, the open conduit has a slightly better

fit (Table 3) and explains tilt displacements from the 2019–20 and 2023 eruptions. The elevation of the geodetic stations at Shishaldin ($\sim$600 m) prevents detection of changes in pressure in the shallowest structures in the edifice (higher than $\sim$600 m above sea level). We propose a conduit that transforms to a dike-like tabular body in the uppermost edifice due to local stress field variations.

This is supported by the tiltmeter observations that show that magma rose from the shallow source into a narrow conduit. Our principal stress analysis indicates that pressurization of the open conduit increased tensile stresses on the NE and SW flanks, facilitating propagation of the summit vent crack. Failure in brittle materials occurs when the tensile stress exceeds the material's tensile strength. While, intact basalt has a tensile strength of $\sim$14 MPa, this value can decrease to 0.1-2.5 MPa for fractured or weakened basaltic rock masses (Schultz, 1995). The principal stress magnitudes across the crack ($\sim$1 MPa) suggests that mechanical failure was possible. Continuous paroxysms during the 2023 eruption may have driven the crack propagation from the crater towards the NE and SW directions. This could also explain the large radius obtained in the open conduit inversion (red circle in Figure 8c), as the conduit geometry may have evolved into a crack in the uppermost portions of the summit during the last stages of the 2023 eruption.

5.2 Magma-tectonic interactions

The inflation and contraction of the magmatic system components likely modulated the stress regime around the edifice as suggested by the modeled increase of Coulomb stress (Figures 8a,b), which is consistent with triggered seismicity on the fault system that previously ruptured in the 1999 M_L 5.2 earthquake. Since the 1999 eruption, the fault system has shown sparse seismicity (e.g., Figure 4a,d and S3b,d). However, seismic events were more frequent in the fault zone during 2013–2018 than in previous years, with magnitudes $M_L < 2$ (Figure S24a). These events fall into the quadrant experiencing positive Coulomb stress change from the pressurization of the shallow source during this period (Figure S24a). During the second inflation period, pressurization caused a stress change of 0.7 bar, coinciding with the M_L 3.6 event on April 20, 2022 (Figures 2e and S24b). Following this, events with magnitudes $M_L > 2$ became more frequent. Our results indicate that conduit depressurization further increased the Coulomb stress change over 1 bar (Figures S24c,d). Although the tectonic setting contributes to these events and we do not model stress change due to the earthquakes themselves, our calculations suggest that magma/fluid flow between the sources influences the stress regime around the edifice and interacted with this fault system.

5.3 Implications for future unrest

The multidisciplinary datasets presented here improve our understanding of Shishaldin's precursory activity. Although certain processes within the magmatic plumbing system are not fully explained, we propose mechanisms consistent with the observations before, during, and after the 2014–15, 2019–20, and 2023 eruptions,

offering a reference for future volcanic unrest.

The increases in the diffuse thermal anomaly during 2010–2013, 2018–2019, and 2022–2023 precede the 2014–2015, 2019–2020, and 2023 eruptions, respectively. These thermal increases may reflect enhanced percolation of magmatic volatiles from the conduit and shallow storage zones through permeable sectors of the upper volcanic edifice; such percolation may promote shallow subsurface condensation of H_2O, accompanied by latent heat release (García-Martínez, Girona, & Benavente, 2025; Girona et al., 2021; Lundgren et al., 2020). This mechanism could also account for the increasing thermal anomalies observed prior to the 2009 unrest episode (Figures 2a,c).

Importantly, the diffuse thermal anomalies preceding the 2014–2015 and 2019–2020 eruptions emerged approximately two years before the onset of magma-intrusion-related deformation (Figure 2c). This time lag suggests that the initiation of thermal unrest and seismic swarms marked the beginning of magma accumulation at shallow levels, even though this early accumulation was not yet sufficient to produce measurable surface deformation. As magma progressively accumulated, pressure within the shallow reservoir increased accordingly; and once this pressure surpassed a critical threshold, it produced a deformation signal detectable by geodetic measurements. In contrast, the rise in diffuse thermal anomalies preceding the 2023 eruption coincided with a period of deflation. This apparent decoupling may be explained by the fact that deformation during this episode was not primarily driven by magma intrusion into the shallow storage zone, but instead by the deflation of a deeper magmatic source, as indicated by geodetic inversions (Table 1 and Figure S13).

Shishaldin's seismicity consists of mostly LP, VT and broadband tremor. Previous analyses of LP swarms between 2001–2004, associated these signals with (1) a repeating and non-destructive source process, (2) shallow degassing processes (Caplan-Auerbach & Petersen, 2005; Cusano et al., 2015; Petersen, 2007; Petersen et al., 2005). While it is difficult to pinpoint an exact LP generation mechanism, we can associate the LP swarms with magma residing shallowly within the conduit of Shishaldin. The location of LPs during swarms between 2005–2012 concentrate in the inferred conduit region of Shishaldin (pink dots in Figures 4, and S3). VT swarms occur in predominantly brittle regimes, presumably due to cooling of conduit wall rocks as the magma ceiling recedes and thermal insulation diminishes, increasing the likelihood of rock fracture (Jolly, Page, & Power, 1994; Schulte-Pelkum & Haney, 2024). Alternatively, VT swarms could result from the solidification of stalled magma within the conduit, sealing fluid flow pathways and promoting pressure accumulation and eventual rock or plug failure within the system (White & McCausland, 2019). Although not documented in the AVO catalog, VOISS-Net finds that background LP activity occurs intermittently during periods of low volcanic activity or repose (e.g., 2004–13 and 2016–19), which contrasts with periods of active eruption dominated by broadband tremor (Figure 5). We contend that quasi-stable bubble nucleation and coalescence, or unsteady fluid flow drive LP activity at Shishaldin, which then switches to more turbulent and rapid gas expulsion processes that drive tremor near

the surface during eruptions. A near real-time VOISS-Net classification could detect these transitions months prior to future eruption onsets.

The inflation episodes are likely associated with intrusion-driven pressurization of the shallow source (2–4 km bsl). However, we do not observe deflation during the 2014–15 and 2019–20 eruptions. Several mechanisms could explain this behavior: (1) a constant magma intrusion rate between eruptions could compensate for pressure losses due to extruded material; (2) the erupted volumes were not large enough to contract the plumbing system, especially if it contained highly compressible magma (e.g., Rivalta & Segall, 2008); and (3) a viscoelastic response of the wall rock and frequent magma intrusions would produce small deflation rates. Our inferred extruded lava volumes suggest that most of the intruded magma in 2013–15 remained stored (Figure S1, and Table 1), making (2) the most likely explanation for the lack of post-eruption deflation. For the 2019–20, the similarity of intruded and extruded volumes ($\sim 3\,\mathrm{Mm}^3$) is consistent with mechanism (1). However, mechanism (3) cannot be ruled out to at least be contributing for either eruption. Future thermo-mechanical coupled models and longer geodetic time series will be necessary to discern the mechanisms responsible (Townsend, 2022), as will be the appropriate treatment of topography (Crozier et al., 2023).

The nature of deformation between mid-2020 and mid-2022 is unclear. Radial deformation at AV36 suggests inflation from 2021–2023 (Figure 2b), but this cannot be confirmed due to data gaps at AV37 and AV39. The deflation trend at AV37 began in late 2022 and early 2023, several months before the onset of the 2023 eruption (July 2023). We hypothesize that small, deep magma intrusions between 2020 and 2022 (undetectable by the geodetic network) may have remobilized the highly compressible magma in the system. As a result, the deepest portions of the conduit (6–12 km bsl) contracted as a significant portion of the magma ascended, not producing significant inflation as volatiles exsolution occurred during ascent, making the magma highly compressible. Regardless of the deformation mechanisms, the geodetic network indicates that Shishaldin deforms months prior to eruption onsets, consistent with pre-eruptive magma recharge timescales inferred from Shishaldin geochemistry (Rasmussen et al., 2018). Previous efforts using InSAR may have missed deformation episodes as the snow cover on the upper edifice inhibits observations where deformation is significant and the wavelengths of most SAR missions are not sensitive enough (C-band can detect LOS deformation > 2.58 cm). Consequently, Shishaldin was interpreted as a non-deforming, open-system volcano (Cusano et al., 2015; Lu & Dzurisin, 2014), reinforcing the need for a continued, long-term in-situ geodetic network to detect future unrest episodes.

6 Conclusions

In this study, we analyze multidisciplinary data for the 2014–15, 2019–20, and 2023 eruptions of Shishaldin Volcano, Alaska. The radiative power obtained from the thermal anomalies show that the 2023 eruption was the most powerful eruption, followed

by the 2019–20 eruption and the 2014–15 eruption. The multiyear brightness temperature of the flanks of the volcano increases between 1–2 °C prior to every eruption. The SO_2 emission rates indicate similar higher magma inputs for the 2014-2015 and 2023 eruptions compared to the 2019–20 eruptions. According to the AVO catalog, VT seismicity rate between 2012–2022 has been lower than in the previous decade suggesting a warm and well-established magmatic system. Many seismic swarms after the 1999 eruption are located close to Shishaldin's vent and most events have depths that are shallower than 2 km. The classification of these events indicates increases of LP events during inter-eruptive periods, likely associated with pre- or post-eruptive degassing activity. The GNSS time series highlight two inflation episodes before the 2014–15 and 2019–20 eruptions and a deflation episode before and during the 2023 eruption. Bayesian inversions indicate that pressurization of a shallow spherical source at 2–4 km bsl depth dominates the inflation episodes and contraction of a 10 km long conduit was the source of the deflation episode. We jointly analyze tiltmeter records related to volcanic events, such as a lava drainage event in September 2019, and two paroxysms in October and November 2023, to constrain the geometry of the open conduit. The results indicate a 1–1.5 km long conduit with a radius of 150 m and a centroid at sea level. We model the tilt time series prior to the lava drainage event where a magma with bubbles growing due to water mass transfer best fits the time-dependent observations. We propose a conceptual model for Shishaldin Volcano consisting of a long and wide conduit, a shallow source at 2–4 km bsl depth and a narrow conduit in the last kilometer that reached the surface (Figure 8). Gas and alternative geodetic models suggest a deep source ($\sim$10 km bsl). These sources increased the Coulomb stress change for the fault system that caused the M_L 5.2 earthquake on March 4, 1999 and the shallow conduit contributed to the propagation of a crack in the NE-SW direction that appeared in the last stages of the 2023 eruption. Our study highlights the importance of long-term, ground-based geophysical network observations as some of the findings presented here depend on subtle changes remote sensing techniques cannot resolve. In particular, the detection of volcanic deformation at this open-system volcano has fundamentally revised our understanding of its magmatic system.

7 Declarations

Funding. This work was funded by the NSF PREEVENTS grants No. 1855126 and 2019232. This material is based upon work supported by the U.S. Geological Survey under Cooperative Agreement No. G21AC10384 and G24AC00240. Any use of trade, firm, or product names is for descriptive purposes only and does not imply endorsement by the U.S. Government.

Data availability. The GNSS and tilt and seismic data is available via EarthScope Consortium Web Services (https://www.unavco.org/data/gps-gnss/data-access-methods/dai1, http://tilt.unavco.org/tilt/ and http://ds.iris.edu/mda/AV/). The TROPOMI SO_2, Sentinel-1 and ERS-1/2 data products are available using the Copernicus Data Space Ecosystem catalogue (https://dataspace.copernicus.eu/analyse/apis/catalogue-apis). ALOS-1 imagery is accesible through the ASF DAAC (https://search.asf.alaska.edu/). MODIS and VIIRS imagery is available on the LP DAAC

(https://search.earthdata.nasa.gov/search). The preprocessed datasets are available in the Angarita et al. (2026) Zenodo repository.

Code availability. The VMOD source code is available at https://github.com/uafgeotools/vmod. The source code to infer elevation values from SAR amplitude imagery is available at https://github.com/mfangaritav/MOSART. The VOISS-Net generalized seismic model and related code are available at https://github.com/darren-tpk/VOISS-Net. The trained HotLINK model can be found at (https://github.com/csaundersshultz/HotLINK). InSAR interferograms were processed with GMTSAR (Sandwell et al., 2011), ISCE-2 (Rosen et al., 2012), and Hyp3 (Hogenson et al., 2016). Deformation time series are obtained using MintPy (Yunjun et al., 2019). PyGMT (Uieda et al., 2021) and Matplotlib (Hunter & Dale, 2007) were used to make figures in this paper.

Competing interests. The authors declare that they have no known competing financial interests or personal relationships that could have appeared to influence the work reported in this paper.

Author contribution. **Mario Angarita:** Conceptualization, Methodology, Software, Validation, Formal Analysis, Investigation, Data Curation, Writing - Original Draft, Writing - Review & Editing, Visualization, Supervision. **Ronni Grapenthin:** Conceptualization, Methodology, Software, Validation, Formal Analysis, Investigation, Data Curation, Writing - Review & Editing, Supervision, Funding Acquisition. **Darren Tan:** Formal Analysis, Investigation, Data Curation, Writing - Review & Editing. **Pablo Saunders-Shultz:** Investigation, Data Curation, Writing - Review & Editing. **Társilo Girona:** Investigation, Data Curation, Writing - Review & Editing. **Revathy M. Parameswaran:** Investigation, Data Curation, Writing - Review & Editing. **Taryn Lopez:** Investigation, Data Curation, Writing - Review & Editing, Funding Acquisition. **Pavel E. Izbekov:** Writing - Review & Editing, Funding Acquisition. **David Fee:** Writing - Review & Editing, Funding Acquisition. **Vanesa Burgos:** Writing - Review & Editing. **Jamshid A. Moshrefzadeh:** Writing - Review & Editing. **Tara Shreve:** Writing - Review & Editing. **Jessica Larsen:** Writing - Review & Editing, Funding Acquisition.

Acknowledgements. We would like to acknowledge the NSF PREEVENTS Eruption Forecasting collaborators for valuable feedback and exchange of ideas and the AVO staff who contributed to the earthquake cataloging and maintenance of the geophysical network.

References

Altamimi, Z., Rebischung, P., Métivier, L., Collilieux, X. (2016). ITRF2014: A new release of the International Terrestrial Reference Frame modeling nonlinear station motions. *Journal of geophysical research: solid earth*, *121*(8), 6109–6131,

Angarita, M., Grapenthin, R., Henderson, S., Christoffersen, M., Anderson, K.R. (2024). Versatile Modeling Of Deformation (VMOD) inversion framework:

Application to 20 years of observations at Westdahl volcano and Fisher Caldera, Alaska, us. *Geochemistry, Geophysics, Geosystems*, *25*(4), e2023GC011341,

Angarita, M., Grapenthin, R., Plank, S., Meyer, F.J., Dietterich, H. (2022). Quantifying large-scale surface change using SAR amplitude images: Crater morphology changes during the 2019–2020 Shishaldin volcano eruption. *Journal of Geophysical Research: Solid Earth*, *127*(8), e2022JB024344,

Angarita, M., Grapenthin, R., Tan, P.K.D., Saunders-Shultz, P., Girona, T., Mozhikunnath Parameswaran, R., ... Larsen, J. (2026, February). *Multidisciplinary perspectives on shishaldin volcano: An open-system, deforming volcano.* Zenodo. Retrieved from https://doi.org/10.5281/zenodo.17808622

Aster, R.C., Borchers, B., Thurber, C.H. (2018). *Parameter estimation and inverse problems*. Amsterdam, Netherlands: Elsevier.

Battista, G., Pavoni, S., Vanali, M. (2024). Compensation of thermal effects on tiltmeter measurements with Moving Least Squares. *IEEE Transactions on Instrumentation and Measurement*, ,

Bertiger, W., Bar-Sever, Y., Dorsey, A., Haines, B., Harvey, N., Hemberger, D., ... others (2020). GipsyX/RTGx, a new tool set for space geodetic operations and research. *Advances in space research*, *66*(3), 469–489,

Cameron, C., Dixon, J., Waythomas, C., Iezzi, W., A.M., K.L., R., McGimsey, Bull, K. (2020). *2016 volcanic activity in Alaska—summary of events and response of the Alaska Volcano Observatory* (Tech. Rep.). US Geological Survey.

Cameron, C.E., Dixon, J.P., Neal, C.A., Waythomas, C.F., Schaefer, J.R., McGimsey, R.G. (2017). *2014 volcanic activity in Alaska: Summary of events and response of the Alaska Volcano Observatory* (Tech. Rep.). US Geological Survey.

Caplan-Auerbach, J., & McNutt, S.R. (2003). New insights into the 1999 eruption of Shishaldin volcano, Alaska, based on acoustic data. *Bulletin of Volcanology*, *65*, 405–417,

Caplan-Auerbach, J., & Petersen, T. (2005). Repeating coupled earthquakes at Shishaldin Volcano, Alaska. *Journal of Volcanology and Geothermal Research*, *145*(1-2), 151–172,

Chaussard, E., Amelung, F., Aoki, Y. (2013). Characterization of open and closed volcanic systems in Indonesia and Mexico using InSAR time series. *Journal of Geophysical Research: Solid Earth*, *118*(8), 3957–3969,

Chouet, B. (1988). Resonance of a fluid-driven crack: Radiation properties and implications for the source of long-period events and harmonic tremor. *Journal of Geophysical Research: Solid Earth*, *93*(B5), 4375–4400,

Christoffersen, M., Grapenthin, R., Angarita, M., Aster, R., Chaput, J., Kyle, P. (2025). Inferring eruption dynamics from seismometer tilt: A case study of Erebus and Augustine volcanoes. *Journal of Geophysical Research: Solid Earth*, *130*(4), e2024JB030657,

Coppola, D., Laiolo, M., Piscopo, D., Cigolini, C. (2013). Rheological control on the radiant density of active lava flows and domes. *Journal of Volcanology and Geothermal Research*, *249*, 39–48,

Crozier, J., Karlstrom, L., Montgomery-Brown, E., Angarita, M., Cayol, V., Bato, M.G., ... others (2023). Understanding the drivers of volcano deformation through geodetic model verification and validation. *Bulletin of Volcanology*, *85*(12), 74,

Cusano, P., Palo, M., West, M. (2015). Long-period seismicity at Shishaldin volcano (Alaska) in 2003–2004: Indications of an upward migration of the source before a minor eruption. *Journal of volcanology and geothermal research*, *291*, 14–24,

Dixon, J., Cameron, A., C.E.and Iezzi, Wallace, K. (2017). *2015 Volcanic activity in Alaska—Summary of events and response of the Alaska Volcano Observatory* (Tech. Rep.). US Geological Survey.

Dow, J.M., Neilan, R.E., Rizos, C. (2009). The international GNSS service in a changing landscape of global navigation satellite systems. *Journal of geodesy*, *83*, 191–198,

Fee, D., Tan, D., Haney, M., Merritt, K., Lyons, J., Wech, A., ... Scamfer, L. (This issue). Seismic and infrasound signals from the 2023 explosive eruption sequence of Shishaldin Volcano. *Bulletin of Volcanology*, ,

Fee, D., Tan, D., Lyons, J., Sciotto, M., Cannata, A., Hotovec-Ellis, A., ... others (2025). A generalized deep learning model to detect and classify volcano seismicity. *Volcanica*, *8*(1), 305–323,

Fioletov, V.E., McLinden, C.A., Griffin, D., Krotkov, N.A., Li, C., Joiner, J., ... Carn, S. (2023). Estimation of anthropogenic and volcanic SO2 emissions from satellite data in the presence of snow/ice on the ground. *Atmospheric Measurement Techniques*, *16*(22), 5575–5592,

Fischer, T.P., Morrissey, M.M., Marta Lucía Calvache, V., Diego Gomez, M., Roberto Torres, C., Stix, J., Williams, S.N. (1994). Correlations between SO2 flux and long-period seismicity at Galeras volcano. *Nature*, *368*(6467), 135–137,

Fournelle, J. (1988). The geology and petrology of Shishaldin volcano. *Unimak Island, Aleutian arc, Alaska: The Johns Hopkins University, unpublished Doctoral Dissertation*, *507*, ,

Fournelle, J., & Marsh, B.D. (1991). Shishaldin Volcano: Aleutian high-alumina basalts and the question of plagioclase accumulation. *Geology*, *19*(3), 234–237,

Freymueller, J.T., & West, M.E. (2024). Earthscope Networks in Alaska and Northwestern Canada. *Tectonics and Seismic Structure of Alaska and Northwestern Canada: EarthScope and Beyond*, 3,

Furst, S., Chéry, J., Mohammadi, B., Peyret, M. (2019). Joint estimation of tiltmeters drift and volume variation during reservoir monitoring. *Journal of Geodesy*, *93*, 1137–1146,

García-Martínez, N., Girona, T., Benavente, D. (2025). On steam-driven thermal anomalies at active volcanoes through laboratory and numerical experiments. *Journal of Geophysical Research: Solid Earth*, *130*(9), e2025JB031598,

Genco, R., & Ripepe, M. (2010). Inflation-deflation cycles revealed by tilt and seismic records at Stromboli volcano. *Geophysical Research Letters*, *37*(12), ,

Girona, T., & Brenot, L. (2026). SSTAR: A user-friendly framework for detecting and monitoring subtle thermal precursors to volcanic eruptions - application to shishaldin, alaska. *Earth, Planets, Space*, , (In review)

971

972 Girona, T., Realmuto, V., Lundgren, P. (2021). Large-scale thermal unrest of volca-
973 noes for years prior to eruption. *Nature Geoscience*, *14*(4), 238–241,
974

975 Gomez-Patron, A., Dietterich, H., Schneider, D. (This issue). Using remote sensing
976 to analyze pre- and co- paroxysm processes at shishaldin (aâyadan or sisagux̂)
977 volcano to improve short-term hazard forecasting. *Bulletin of Volcanology*, ,
978

979 Goulty, N.R. (1976). Strainmeters and tiltmeters in geophysics. *Tectonophysics*, *34*(3-
980 4), 245–256,
981

982 Grapenthin, R., Cheng, Y., Angarita, M., Tan, D., Meyer, F.J., Fee, D., Wech, A.
983 (2022). Return from dormancy: rapid inflation and seismic unrest driven by
984 transcrustal magma transfer at Mt. Edgecumbe (l'úx shaa) Volcano, Alaska.
985 *Geophysical Research Letters*, *49*(20), e2022GL099464,
986

987 Grapenthin, R., Kyle, P., Aster, R.C., Angarita, M., Wilson, T., Chaput, J. (2022).
988 Deformation at the open-vent erebus volcano, Antarctica, from more than 20
989 years of GNSS observations. *Journal of Volcanology and Geothermal Research*,
990 *432*, 107703,
991

992 Gudmundsson, M.T., Jónsdóttir, K., Hooper, A., Holohan, E.P., Halldórsson, S.A.,
993 Ófeigsson, B.G., ... others (2016). Gradual caldera collapse at Bárdarbunga vol-
994 cano, Iceland, regulated by lateral magma outflow. *Science*, *353*(6296), aaf8988,
995

996 Hogenson, K., Arko, S.A., Buechler, B., Hogenson, R., Herrmann, J., Geiger, A. (2016).
997 Hybrid Pluggable Processing Pipeline (hyp3): A cloud-based infrastructure for
998 generic processing of SAR data. *Agu fall meeting abstracts* (Vol. 2016, pp.
999 IN21B–1740).

1000 Hunter, J., & Dale, D. (2007). The matplotlib user's guide. *Matplotlib 0.90. 0 user's*
1001 *guide*, *487*, ,
1002

1003 Jolly, A.D., Page, R.A., Power, J.A. (1994). Seismicity and stress in the vicinity of
1004 Mount Spurr volcano, south central Alaska. *Journal of Geophysical Research:*
1005 *Solid Earth*, *99*(B8), 15305–15318,
1006

Kilbride, B.M., Edmonds, M., Biggs, J. (2016). Observing eruptions of gas-rich compressible magmas from space. *Nature Communications*, *7*(1), 13744,

King, G.C., Stein, R.S., Lin, J. (1994). Static stress changes and the triggering of earthquakes. *Bulletin of the Seismological Society of America*, *84*(3), 935–953,

Lerner, A.H., O'Hara, D., Karlstrom, L., Ebmeier, S.K., Anderson, K.R., Hurwitz, S. (2020). The prevalence and significance of offset magma reservoirs at arc volcanoes. *Geophysical Research Letters*, *47*(14), e2020GL087856,

Loewen, M. (This issue). Overview and chronology of the 2023 (and 2019?) eruption of Shishaldin Volcano. *Bulletin of Volcanology*, ,

Lopez, T., Carn, S., Werner, C., Fee, D., Kelly, P., Doukas, M., ... Schneider, D. (2013). Evaluation of Redoubt Volcano's sulfur dioxide emissions by the Ozone Monitoring Instrument. *Journal of Volcanology and Geothermal Research*, *259*, 290–307,

Lopez, T., Kelly, P., Lerner, A., Rasmussen, D. (This issue). Insights into magmatic processes from Shishaldin Volcano based on satellite and airborne volcanic gas measurements. *Bulletin of Volcanology*, ,

Lu, Z., & Dzurisin, D. (2014). *InSAR imaging of Aleutian volcanoes: Monitoring a volcanic arc from space*. Chichester, UK: Springer.

Lundgren, P., Girona, T., Bato, M.G., Realmuto, V.J., Samsonov, S., Cardona, C., ... Aivazis, M. (2020). The dynamics of large silicic systems from satellite remote sensing observations: The intriguing case of Domuyo volcano, Argentina. *Scientific reports*, *10*(1), 11642,

Lundgren, P., Samsonov, S.V., López Velez, C.M., Ordoñez, M. (2015). Deep source model for Nevado del Ruiz Volcano, Colombia, constrained by interferometric synthetic aperture radar observations. *Geophysical Research Letters*, *42*(12), 4816–4823,

Lyons, J.J., Waite, G.P., Ichihara, M., Lees, J.M. (2012). Tilt prior to explosions and the effect of topography on ultra-long-period seismic records at Fuego volcano, Guatemala. *Geophysical research letters*, *39*(8), ,

Mastin, L.G., & Pollard, D.D. (1988). Surface deformation and shallow dike intrusion processes at inyo craters, long valley, california. *Journal of Geophysical Research: Solid Earth*, *93*(B11), 13221–13235,

McGimsey, R.G., & Neal, C.A. (1996). *Volcanic activity in Alaska and kamchatka: Summary of events and response of the Alaska Volcano Observatory 1995* (Tech. Rep.). US Geological Survey.

McGimsey, R.G., Neal, C.A., Girina, O.A., Chibisova, M., Rybin, A. (2014). *2009 Volcanic Activity in Alaska, Kamchatka, and the Kurile Islands: Summary of Events and Response of the Alaska Volcano Observatory* (Tech. Rep.). US Geological Survey.

McTigue, D. (1987). Elastic stress and deformation near a finite spherical magma body: Resolution of the point source paradox. *Journal of Geophysical Research: Solid Earth*, *92*(B12), 12931–12940,

Moran, S., Kwoun, O., Masterlark, T., Lu, Z. (2006). On the absence of InSAR-detected volcano deformation spanning the 1995–1996 and 1999 eruptions of Shishaldin Volcano, Alaska. *Journal of Volcanology and Geothermal Research*, *150*(1-3), 119–131,

Moran, S., Stihler, S., Power, J. (2002). A tectonic earthquake sequence preceding the April–May 1999 eruption of Shishaldin Volcano, Alaska. *Bulletin of Volcanology*, *64*, 520–524,

NASEM, National Academies of Sciences and Medicine and Division on Earth and Life Studies and Board on Earth Sciences and Committee on Seismology and Committee on Improving Understanding of Volcanic Eruptions. (2017). *Volcanic eruptions and their repose, unrest, precursors, and timing*. National Academies Press.

Neal, C., McGimsey, R., Chubarova, O. (2004). *2000 Volcanic Activity in Alaska and Kamchatka: Summary of Events and Response of the Alaska Volcano Observatory* (Tech. Rep.). US Geological Survey.

Neal, C., McGimsey, R., Dixon, J., Melnikov, D. (2005). *2004 Volcanic Activity in Alaska and Kamchatka: Summary of Events and Response of the Alaska Volcano Observatory* (Tech. Rep.). US Geological Survey.

Nishimura, T. (2009). Ground deformation caused by magma ascent in an open conduit. *Journal of Volcanology and Geothermal Research*, *187*(3-4), 178–192,

Nye, C., Keith, T., Eichelberger, J., Miller, T., McNutt, S., Moran, S., ... Schaefer, J. (2002). The 1999 eruption of Shishaldin Volcano, Alaska: monitoring a distant eruption. *Bulletin of volcanology*, *64*, 507–519,

Okada, Y. (1985). Surface deformation due to shear and tensile faults in a half-space. *Bulletin of the seismological society of America*, *75*(4), 1135–1154,

Orr, T.R., Cameron, C.E., Dietterich, H.R., Dixon, J.P., Enders, M.L., Grapenthin, R., ... others (2023). *2019 Volcanic activity in Alaska—Summary of events and response of the Alaska Volcano Observatory* (Tech. Rep.). US Geological Survey.

Orr, T.R., Cameron, C.E., Dietterich, H.R., Loewen, M.W., Lopez, T., Lyons, J., ... Waythomas, C. (2024). *2020 Volcanic Activity in Alaska—Summary of Events and Response of the Alaska Volcano Observatory* (Tech. Rep.). US Geological Survey.

Pérez-Estay, N., Ruz-Ginouves, J., Pérez-Flores, P., Sielfeld, G., Roquer, T., Cembrano, J. (2023). Decoding the state of stress and fluid pathways along the andean southern volcanic zone. *Communications Earth & Environment*, *4*(1), 390,

Petersen, T. (2007). Swarms of repeating long-period earthquakes at Shishaldin Volcano, Alaska, 2001–2004. *Journal of Volcanology and Geothermal Research*, *166*(3-4), 177–192,

Petersen, T., Caplan-Auerbach, J., McNutt, S.R. (2005). Sustained long-period seismicity at Shishaldin Volcano, Alaska. *Journal of Volcanology and Geothermal Research*, *151*(4), 365–381,

Petersen, T., & McNutt, S.R. (2006). Seismo-acoustic signals associated with degassing explosions recorded at Shishaldin Volcano, Alaska, 2003–2004. *Bulletin of Volcanology*, *69*, 527–536,

Rasmussen, D.J., Plank, T.A., Roman, D.C., Power, J.A., Bodnar, R.J., Hauri, E.H. (2018). When does eruption run-up begin? Multidisciplinary insight from the 1999 eruption of Shishaldin volcano. *Earth and Planetary Science Letters*, *486*, 1–14,

Reeder, J. (1990). Shishaldin in:. *Annual report of the world volcanic eruptions in 1986*, 36,

Rivalta, E., & Segall, P. (2008). Magma compressibility and the missing source for some dike intrusions. *Geophysical Research Letters*, *35*(4), ,

Robinson, D., & Estilow, T. (2012). *NOAA climate data record (CDR) of Northern Hemisphere (NH) Snow Cover Extent (SCE) version 1. NOAA National Centers for Environmental Information.*

Rosen, P.A., Gurrola, E., Sacco, G.F., Zebker, H. (2012). The InSAR scientific computing environment. *Eusar 2012; 9th european conference on synthetic aperture radar* (pp. 730–733).

Sakata, S., & Sato, H. (1986). Borehole-type tiltmeter and three-component strainmeter for earthquake prediction. *Journal of Physics of the Earth*, *34*(Supplement), S129–S140,

Sandwell, D., Mellors, R., Tong, X., Wei, M., Wessel, P. (2011). *Gmtsar: An InSAR processing system based on generic mapping tools* (Tech. Rep.). UC San Diego.

Saunders-Shultz, P., Lopez, T., Dietterich, H., Girona, T. (2024). Automatic identification and quantification of volcanic hotspots in Alaska using HotLINK: the hotspot learning and identification network. *Frontiers in Earth Science*, *12*, 1345104,

Schulte-Pelkum, V., & Haney, M.M. (2024). Fault–dike–magma interactions inferred from transcrustal conical structures under Akutan volcano. *Seismological Research Letters*, *95*(5), 2663–2673,

Schultz, R. (1995). Limits on strength and deformation properties of jointed basaltic rock masses. *Rock Mechanics and Rock Engineering*, *28*, 1–15,

Shackelford, D. (1978). Shishaldin in:. *Annual report of the world volcanic eruptions in 1976*, ,

Siebert, L., Simkin, T., Kimberly, P. (2010). *Volcanoes of the World.* Berkeley, California: Univ of California Press.

Stelling, P., Beget, J., Nye, C., Gardner, J., Devine, J., George, R. (2002). Geology and petrology of ejecta from the 1999 eruption of Shishaldin Volcano, Alaska. *Bulletin of Volcanology*, *64*, 548–561,

Tan, D., Fee, D., Witsil, A., Girona, T., Haney, M., Wech, A., ... Lopez, T. (2024). Detection and Characterization of Seismic and Acoustic Signals at Pavlof Volcano, Alaska, Using Deep Learning. *Journal of Geophysical Research: Solid Earth*, *129*(6), e2024JB029194,

Townsend, M. (2022). Linking surface deformation to thermal and mechanical magma chamber processes. *Earth and Planetary Science Letters*, *577*, 117272,

Uieda, L., Tian, D., Leong, W.J., Toney, L., Schlitzer, W., Grund, M., ... Wessel, P. (2021). *PyGMT: A Python interface for the generic mapping tools.* Zenodo.

Vargas-Bracamontes, D., & Neuberg, J. (2012). Interaction between regional and magma-induced stresses and their impact on volcano-tectonic seismicity. *Journal of volcanology and geothermal research*, *243*, 91–96,

White, R.A., & McCausland, W.A. (2019). A process-based model of pre-eruption seismicity patterns and its use for eruption forecasting at dormant stratovolcanoes. *Journal of Volcanology and Geothermal Research*, *382*, 267–297,

Williams, S.D. (2008). CATS: GPS coordinate time series analysis software. *GPS solutions*, *12*, 147–153,

Xiao, Z., Freymueller, J.T., Grapenthin, R., Elliott, J.L., Drooff, C., Fusso, L. (2021). The deep shumagin gap filled: Kinematic rupture model and slip budget analysis of the 2020 Mw 7.8 Simeonof earthquake constrained by GNSS, global seismic waveforms, and floating InSAR. *Earth and Planetary Science Letters*, *576*, 117241,

Yang, X.-M., Davis, P.M., Dieterich, J.H. (1988). Deformation from inflation of a dipping finite prolate spheroid in an elastic half-space as a model for volcanic stressing. *Journal of Geophysical Research: Solid Earth*, *93*(B5), 4249–4257,

Yunjun, Z., Fattahi, H., Amelung, F. (2019). Small baseline InSAR time series analysis: Unwrapping error correction and noise reduction. *Computers & Geosciences*, *133*, 104331,

1193

Supplementary Information for "Multidisciplinary perspectives on Shishaldin Volcano: Open-system, deforming volcano"

We present the fits for the geodetic models used for the GNSS observations (Tables S1–S2), the radiative energy emitted by the thermal anomalies detected with HotLINK and inferred lava extruded volumes (Figure S1), the magnitude of completeness plot for the seismic catalog (Figure S2). The GNSS time series components and the estimated velocities for the deformation episodes are shwon in Figure S5. The posterior distributions for inversions of geodetic data from the different deformation episodes are in Figures S6–S13. The deformation produced by the dual-source model during the deflation episode is shown in Figure S14. The LOS velocities from the Sentinel-1 and ALOS-1 are shown in Figure S15. Elevation changes for the 2023 eruption inferred from the amplitude of TerraSAR-X images are provided in Figure S16. Photographs and seismic records of a rim collapse are shown in Figure S17. The long-term tilt timeseries and instrumental drift and temperature corrections is in Figure S18. The radial tilt displacements associated with volcanic events are shown in Figure S19. The tilt timeseries before the lava drainage event and the three regimes captured in the Nishimura (2009) model are shown in Figure S20. The posterior distributions for the tilt displacements using an open conduit geometry is in Figure S21. Inversion results for tilt displacements associated with paroxysms in the 2023 eruption using a dike geometry are in Figures S22–S23. The Coulomb stress changes produced by the deformation sources is shown in Figure S24. In addition, we provide text explaining the procedure to calculate the low-temperature thermal anomalies (Text S1).

Text S1: Diffuse, low-temperature thermal anomalies

To assess subtle, long-term thermal variations at Shishaldin volcano, we analyzed satellite-based thermal infrared data spanning over two decades. Specifically, we investigated multi-year trends in radiant heat emissions from the volcano's upper flanks using data from the MODIS sensor. The analysis was conducted with the Subtle Surface Thermal Anomaly Recognizer (SSTAR) (Girona and Brenot, 2026), an user-friendly tool that applies an automated median-of-medians algorithm that extends from Girona et al. (2021). Similar methodologies have been applied to other volcanic systems (Lundgren et al., 2020; Reed et al., 2021; Zhan et al., 2022).

Thermal infrared observations were derived from MODIS radiance, geolocation, and cloud-mask products obtained from NASA's Earthdata repository (`https://earthdata.nasa.`

gov/), covering the period from 4 July 2002 to 31 December 2024. We used three primary datasets: (1) MODIS Terra/Aqua Calibrated Radiances 5-Min Level-1B Swath 1 km V006 (MOD021KM/MYD021KM), which provides calibrated, instrument-corrected radiance values; (2) MODIS Terra/Aqua Geolocation Fields 5-Min Level-1A Swath 1 km V006 (MOD03/MYD03), which provides precise scene georeferencing; and (3) MODIS Terra/Aqua Cloud Mask and Spectral Test Results 5-Min Level-2 Swath 1 km V6.1 (MOD35/MYD35), used to identify and exclude cloud-contaminated pixels.

From each scene, we extracted spectral radiance values from cloud-free pixels in MODIS band 31 (10.780–11.280 μm) and converted them to brightness temperature using Planck's function. These values were then used to compute the median brightness temperature within a 4 km^2 region centered on the volcano's summit (54.756°N, 163.970°W). To provide a relative measure of surface heating, we also computed a reference brightness temperature from a surrounding annular region, defined by an inner square (60 km per side) and an outer square (80 km per side), both centered on the crater and extending beyond the volcanic edifice. The analysis incorporated both daytime and nighttime scenes.

To construct a uniformly sampled time series, we calculated the daily median difference between the crater and reference region temperatures. On average, ∼135 days of valid data were available each year, and the resulting gaps were filled using nearest-neighbor interpolation. To isolate long-term trends exceeding one year, we applied a 730-day low-pass median filter (as described in Girona and Brenot, 2026). This approach suppresses short-term fluctuations and seasonal variability, yielding a signal that captures multi-year changes in surface heat emissions at Shishaldin's upper flanks relative to the surrounding region.

Table S1: Root mean square error (RMSE) for the inversions on the deflation episode using the spheroidal and dual spherical models

Episode	Model	RMSE (mm)	# of parameters
Inflation (2013-15)	Spherical	1.0	5
	Dislocation	0.5	8
	Open conduit	1.0	6
Inflation (2018-20)	Spherical	1.0	5
	Dislocation	0.7	8
	Open conduit	1.0	6
Deflation (2022-24)	Spheroid	1.1	8
	Dual sphere	1.1	10

Table S2: F-values between dislocation and spherical models with a sample size of 9 observations (3 stations $\times$ 3 components= 9 observations). The theoretical value is $F(3,1) = 215.7$. In this case, 3 and 1 represent the degrees of freedom for the spherical and dislocation models, respectively

Inflation (2013-15)	Inflation (2018-20)
1.1	0.35

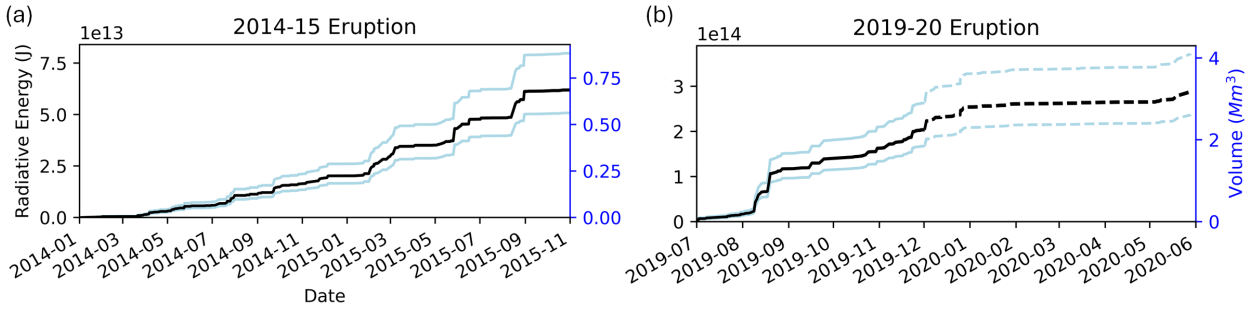

Fig. S1: Radiative energy for the 2019-2020 eruption calculated from the radiative power of the thermal anomalies. Solid lines represent calculations when the eruptive activity was mostly effusive, dashed lines represent calculations when the activity turned explosive. The right y-axis represents the inferred lava flow volumes. Black line represents the radiative energy/lava flow volume and the cyan lines the volume uncertainties.

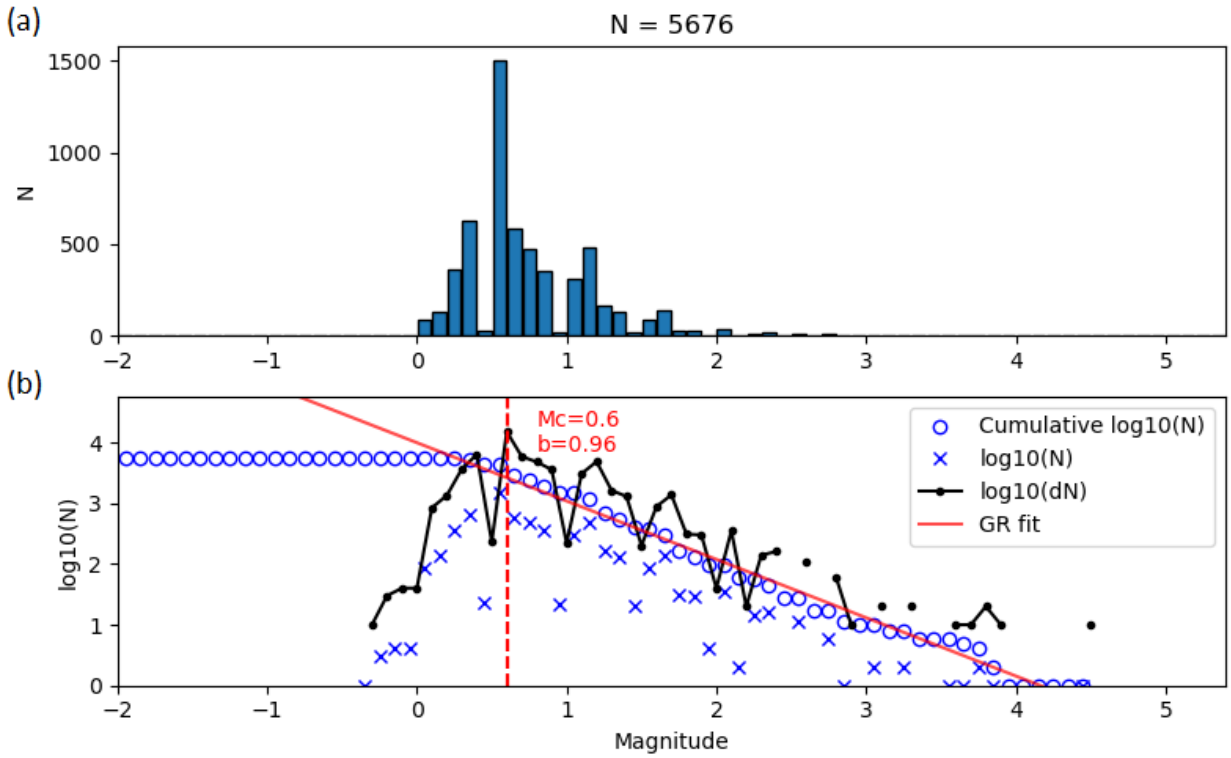

Fig. S2: Magnitude of completeness (M_c) for the AVO earthquake catalog, for events within a radius of 15 km from Shishaldin's vent. (a) Magnitude histogram for events between January 1, 1997 and June 1, 2024, where N denotes earthquake count. (b) Cumulative logarithmic magnitude-frequency distribution (blue circles), logarithmic earthquake count ($\log_{10} N$, blue crosses) and logarithm of the change in event counts between bins ($\log_{10} dN$, black points, connected by a line for visibility). The red solid line shows the best fit for the cumulative distribution and the dashed vertical red line marks the magnitude of completeness. The b-value corresponds to the slope of the Gutenberg-Richter (GR) power-law fit.

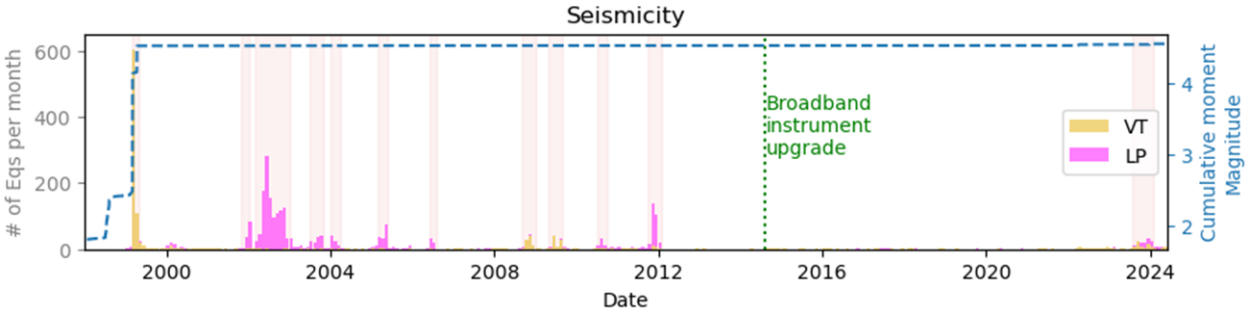

Fig. S3: Earthquake count per month and cumulative moment magnitude between January 1, 1998 and June 1, 2024. The green dotted line the upgrade of the network with broadband instruments on August 7, 2014.

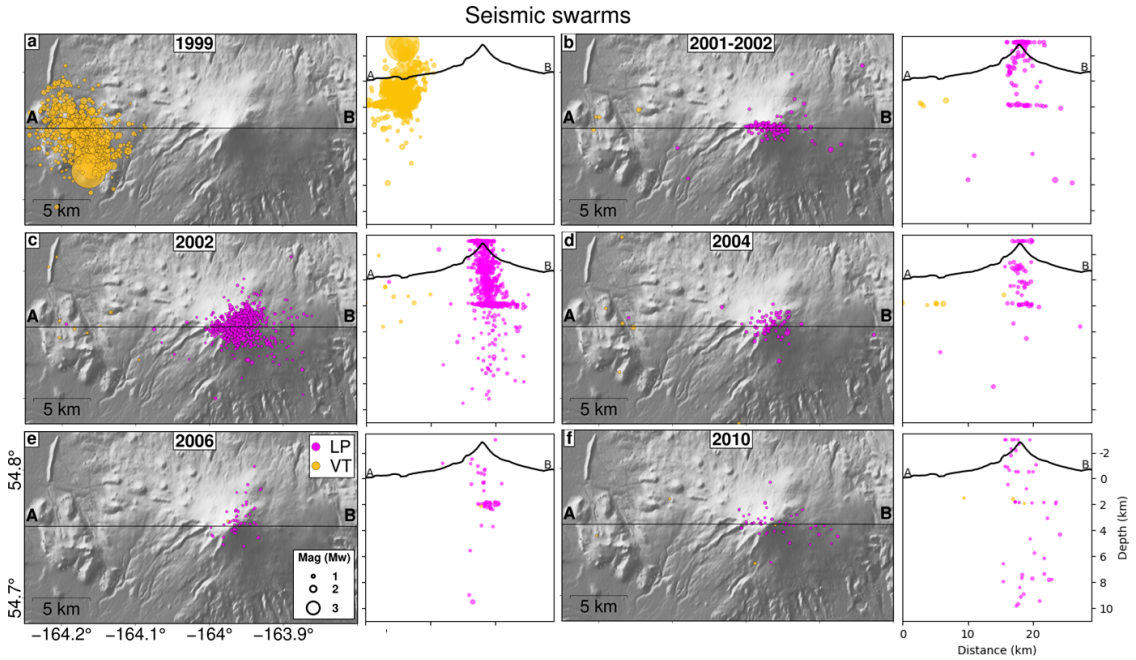

Fig. S4: Seismic swarms since the network became operational between -1–10 km bsl. (a) March 3, 1999 and March 8, 1999, (b) November 1, 2001 and January 15, 2002, (c) March 1, 2002 and December 31, 2002, (d) January 1, 2004 and March 1, 2004 (e) June 1, 2006 and August 1, 2006, (f) July 1, 2010 and October 1, 2010. Left, horizontal location of the hypocenters. Right, vertical projection for the hypocenters in the AB profile (black line) in the left panels. Note that earthquakes that locate above the ground surface are typically artifacts of earthquake location uncertainty, arising from limitations in the seismic velocity model, data quality, or station coverage, rather than true seismic events occurring in the air.

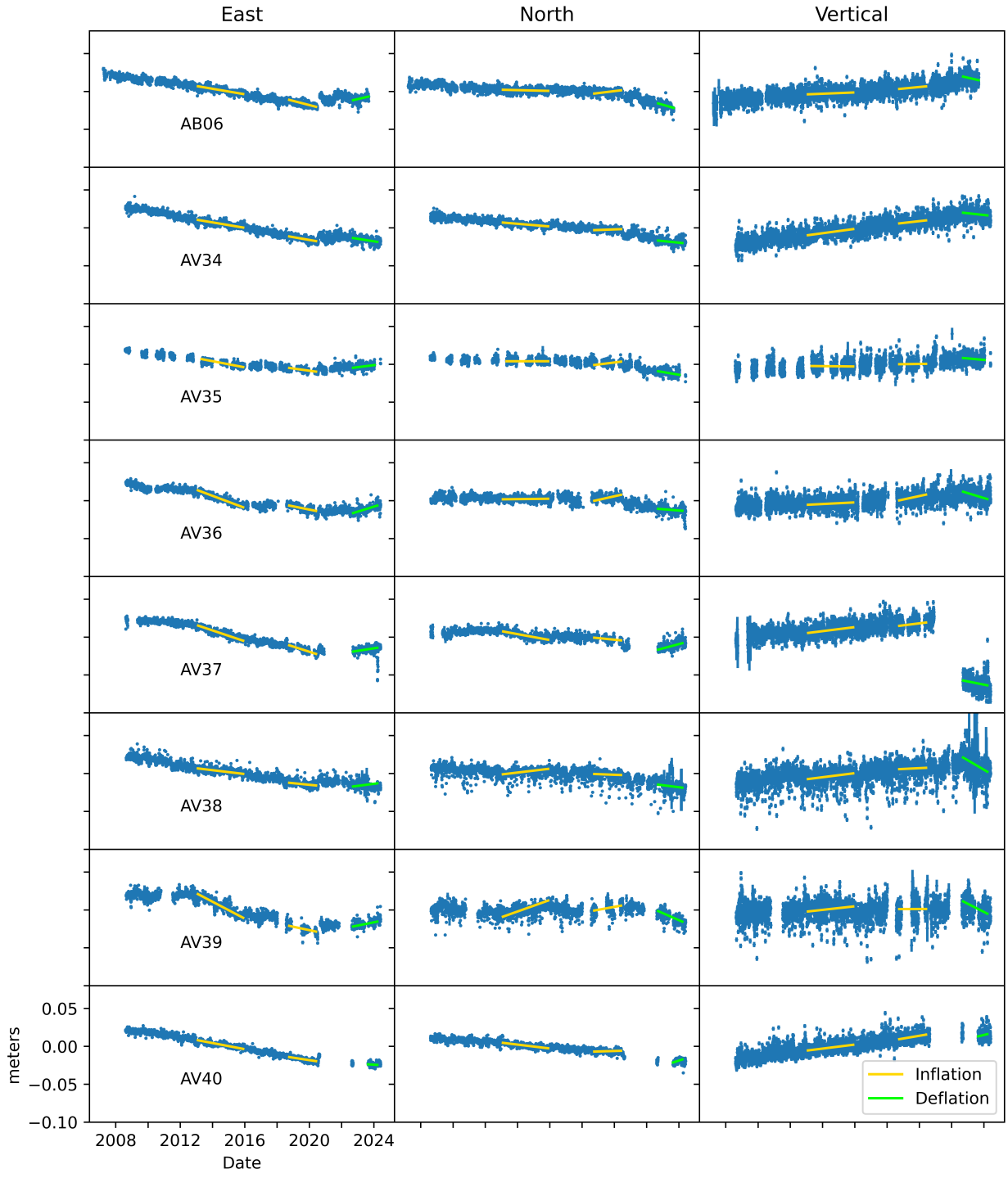

Fig. S5: GNSS daily time series. Blue points represent the daily positions with respect to the North American plate. The gold and green lines represent the trends for the inflation and deflation periods, respectively. The label axes are the same for all columns and rows.

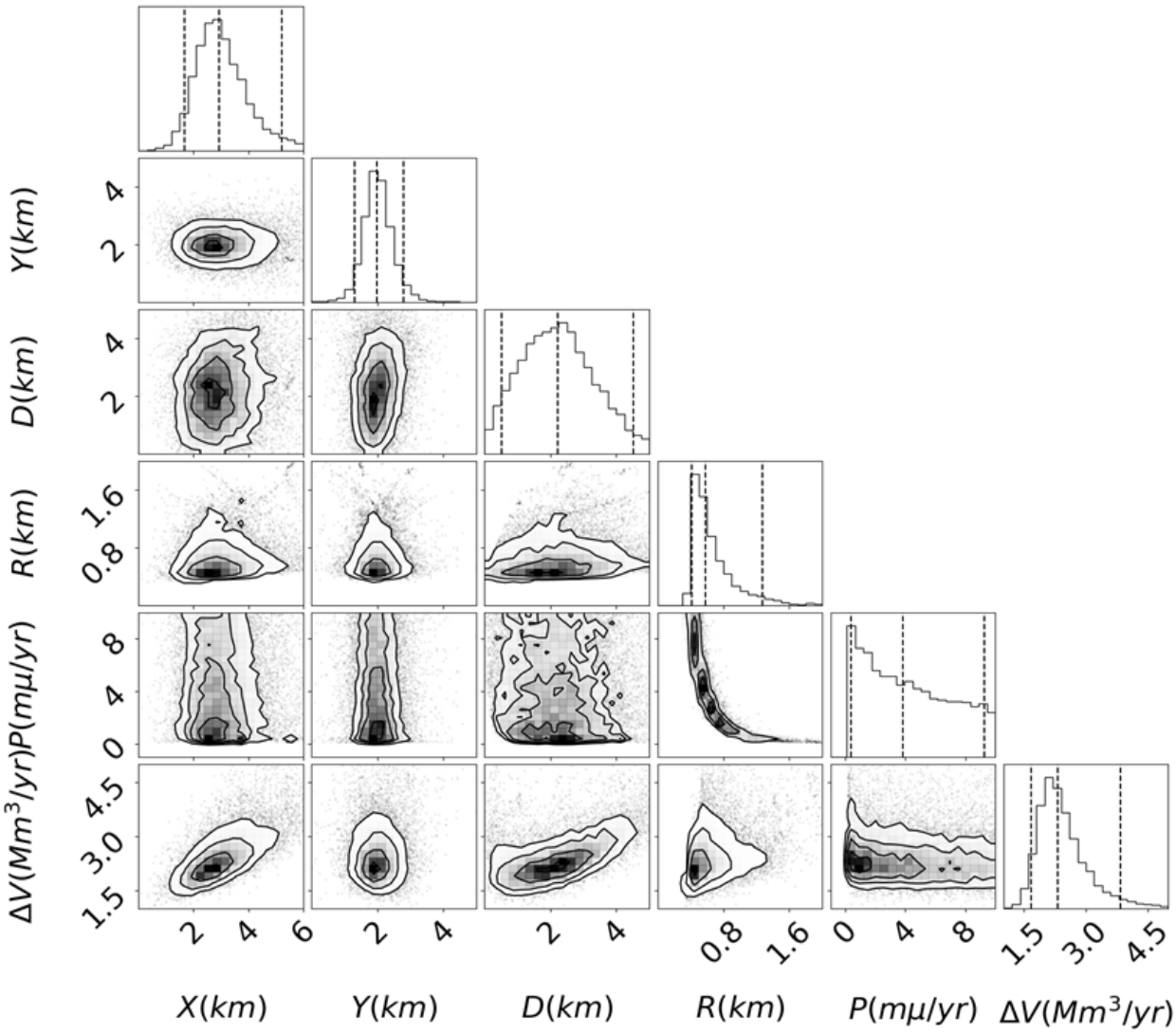

Fig. S6: Posterior distributions (main diagonal), and marginal distributions (off diagonal elements) of model parameters for a spherical source geometry modeling the inflation episode between February, 2013 and November, 2015. X and Y represent horizontal centroid location, D the depth, R the sphere radius, P the pressure change rate and ΔV the inferred volume change rate. Dashed lines in the histograms are the 5th, 50th and 95th percentiles. The parameters of the maximum a priori (MAP) solution are given by darkest points in the distribution when trade-off is not present.

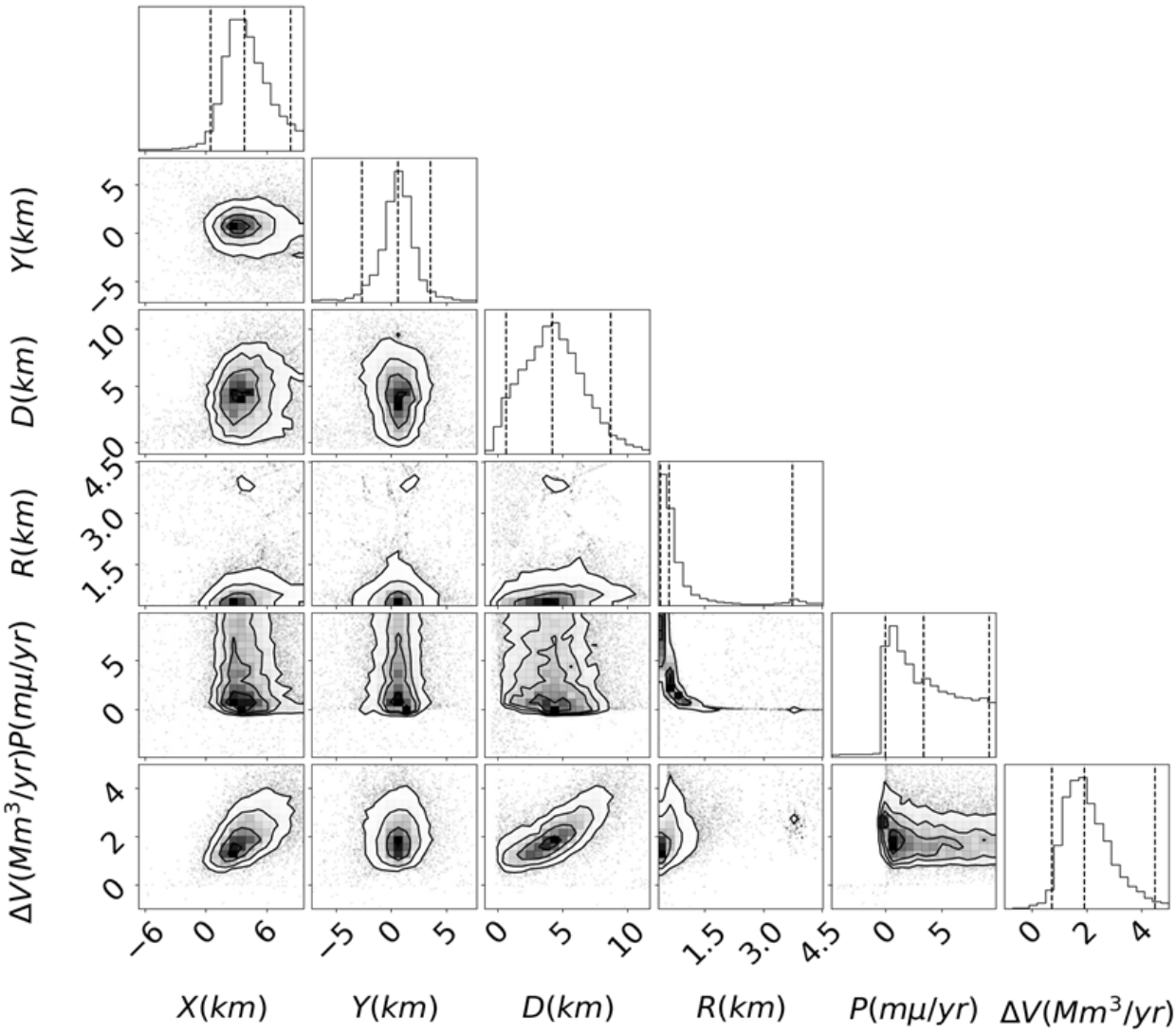

Fig. S7: Same as in Figure S6, but for the inflation episode between October, 2018 and June, 2020.

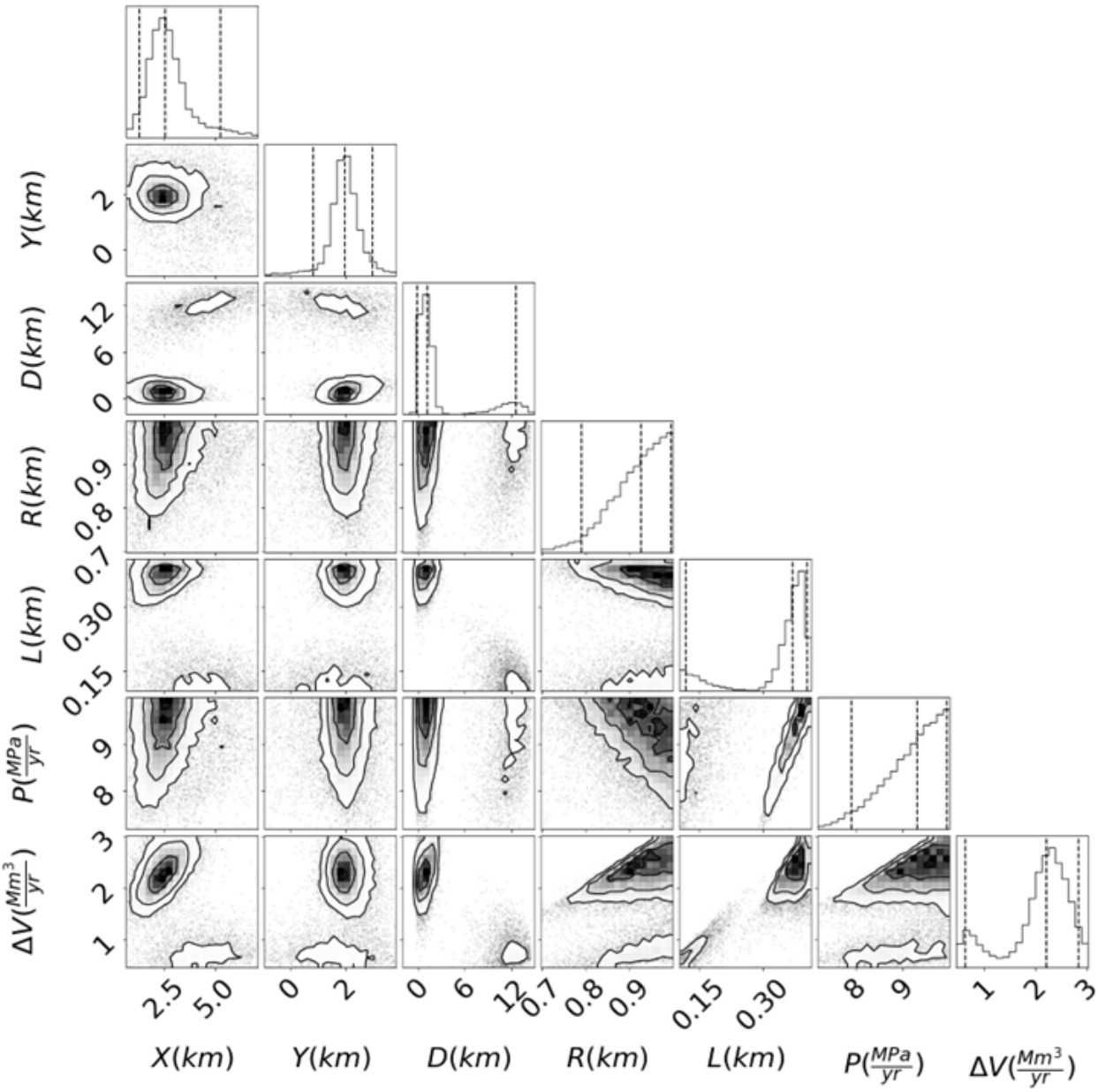

Fig. S8: Same as in Figure S6, but for the inflation episode between February, 2013 and November, 2015 and an open conduit model. X and Y represent horizontal centroid location, D the centroid depth, R the conduit radius, P the pressure change rate and ΔV the inferred volume change rate.

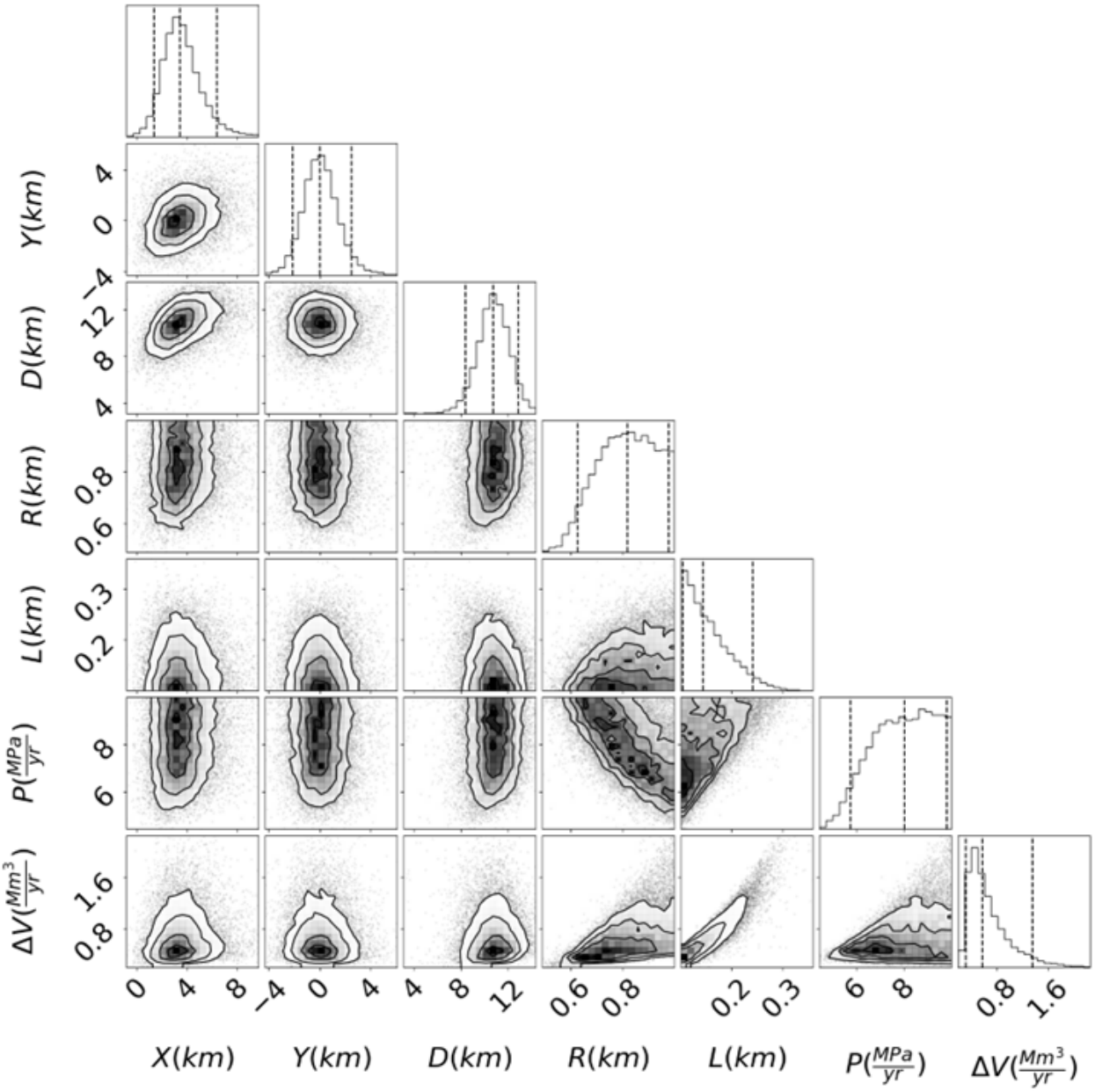

Fig. S9: Same as in Figure S6, but for the inflation episode between October, 2018 and June, 2020 and an open conduit model. The labels are the same as in Figure S8.

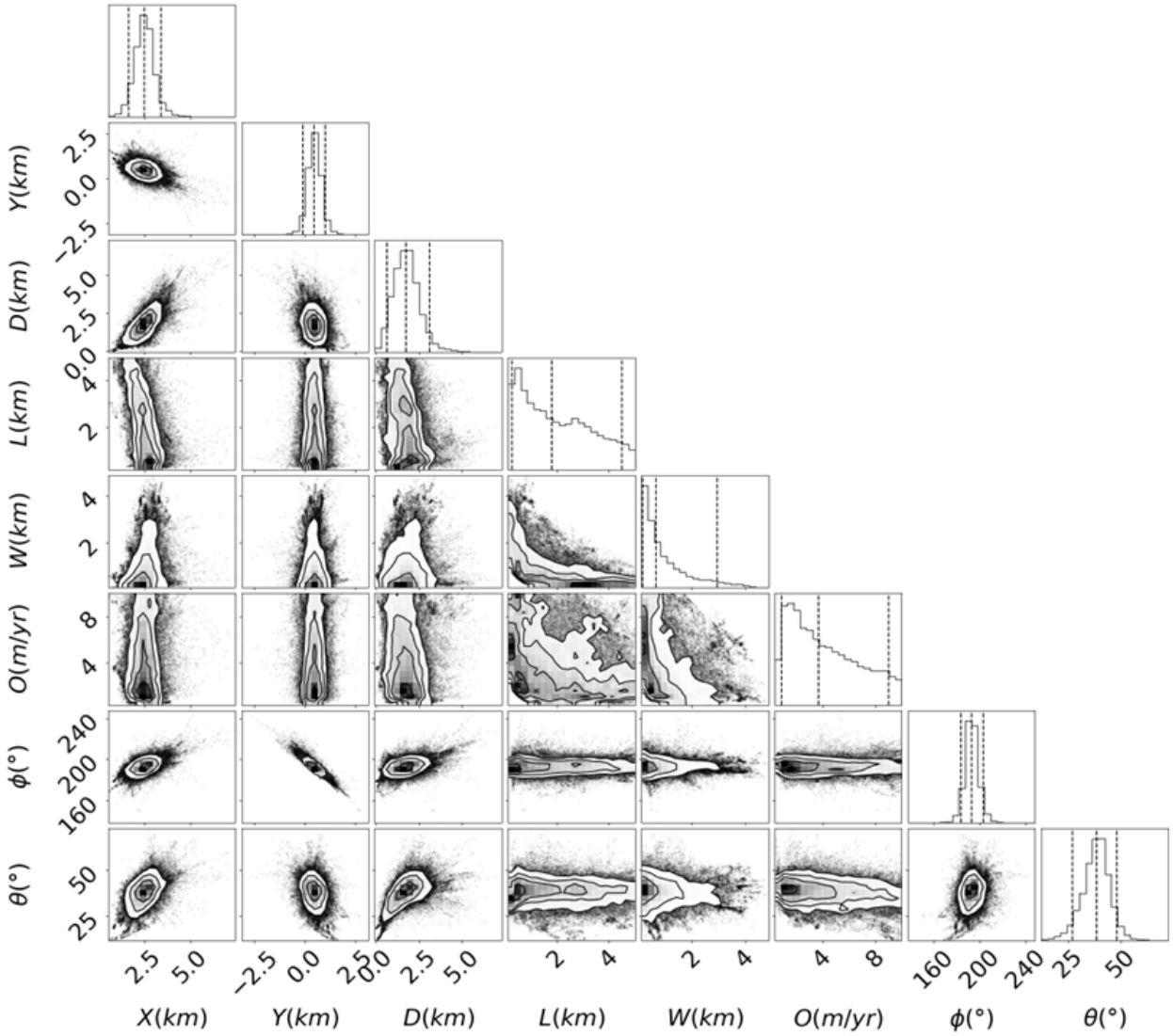

Fig. S10: Posterior distributions for the inflation episode between February, 2013 and November, 2015 and a dislocation model. X and Y represent horizontal centroid location, D the depth, L the dislocation length W the dislocation width, O the opening rate, ϕ the strike, and θ the dipping angle.

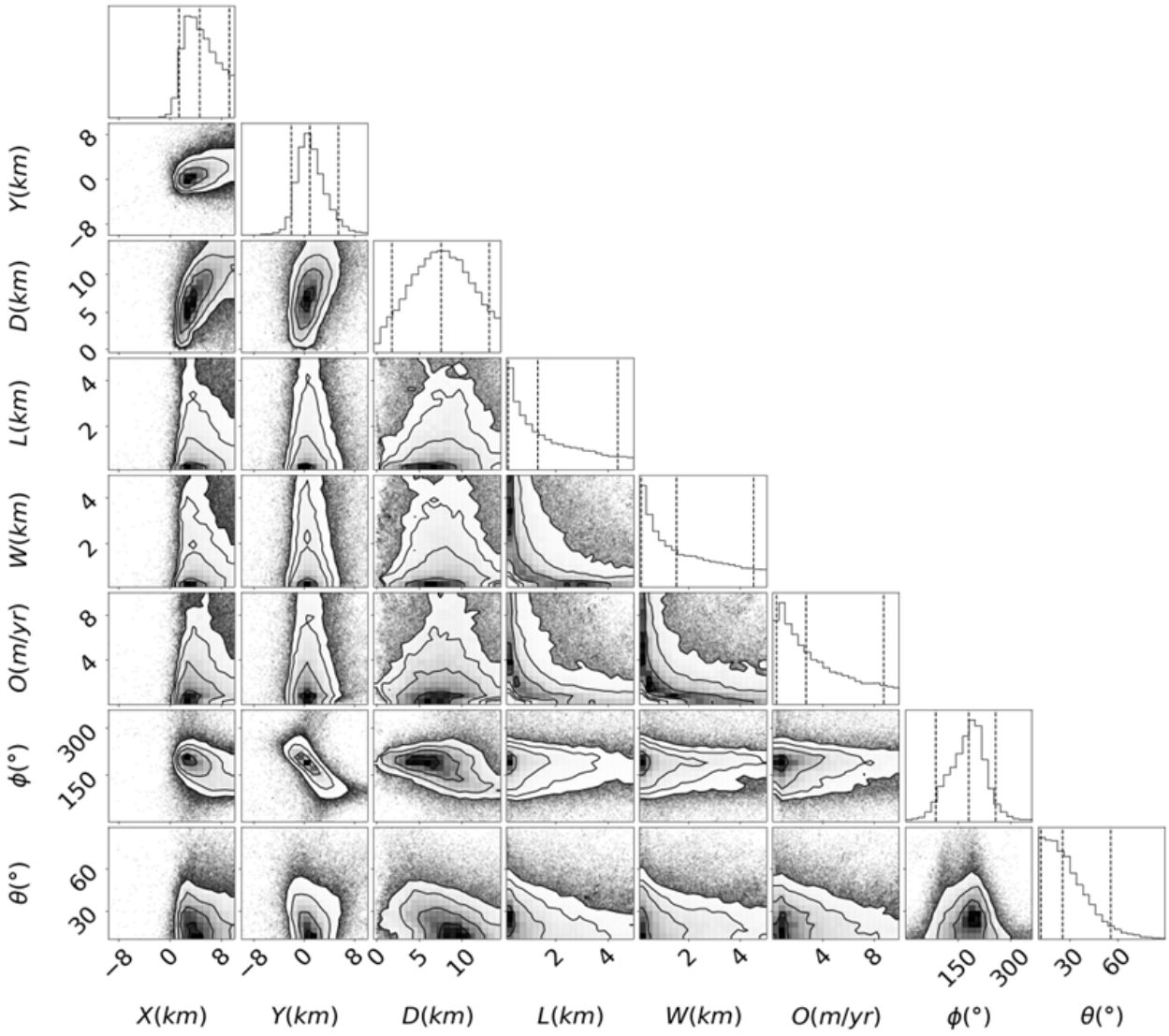

Fig. S11: Posterior distributions for the inflation episode between October, 2018 and June, 2020 and a dislocation model. The labels are the same as in Figure S10.

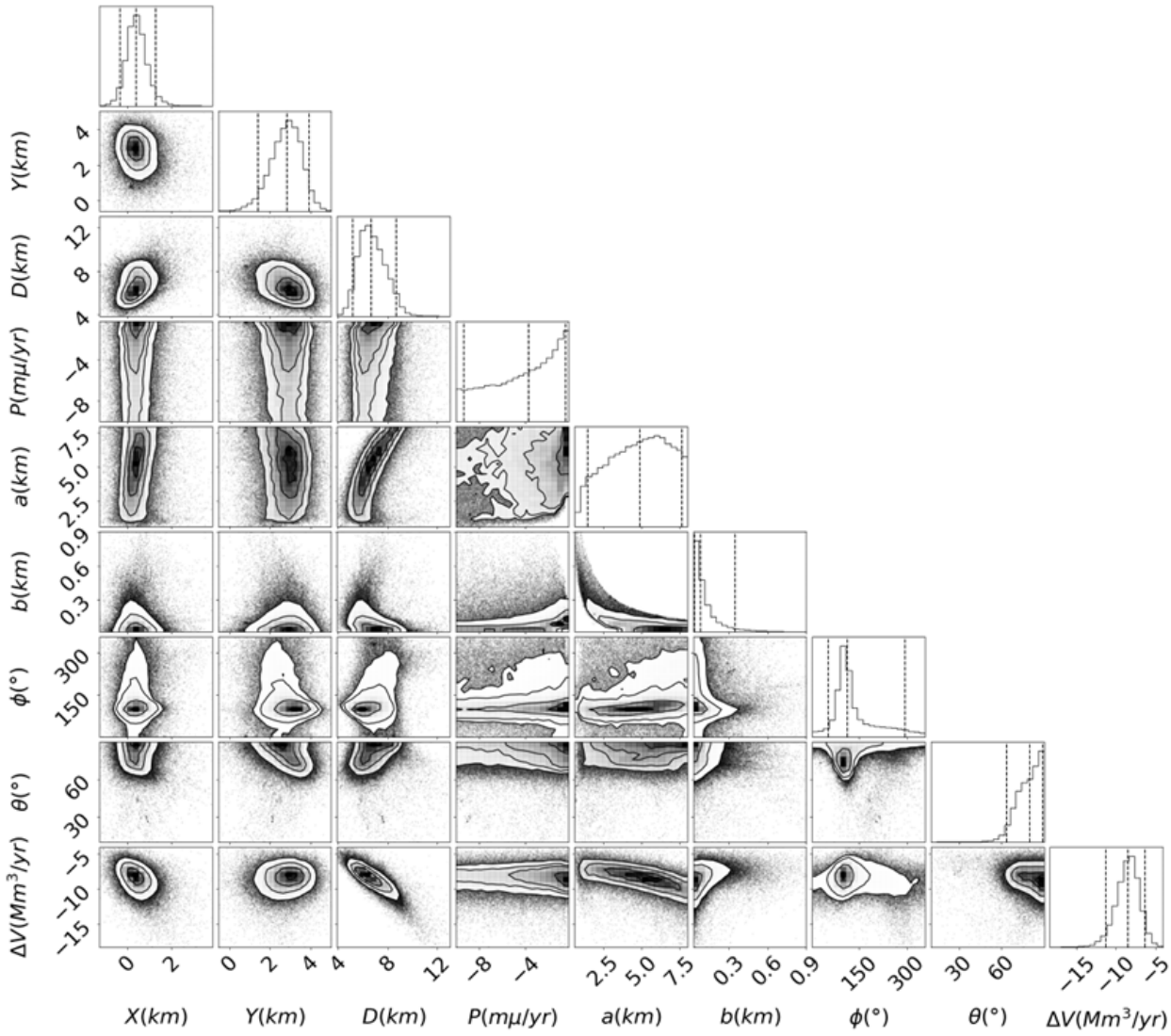

Fig. S12: Posterior distributions for the deflation episode between September 2022 and March 2024 and a spheroidal geometry. X and Y represent horizontal centroid location, D the depth, P the pressure change rate, a the semimajor axis, b the semiminor axis, ϕ is the azimuth angle, θ the dipping angle, and ΔV the inferred volume change rate inferred.

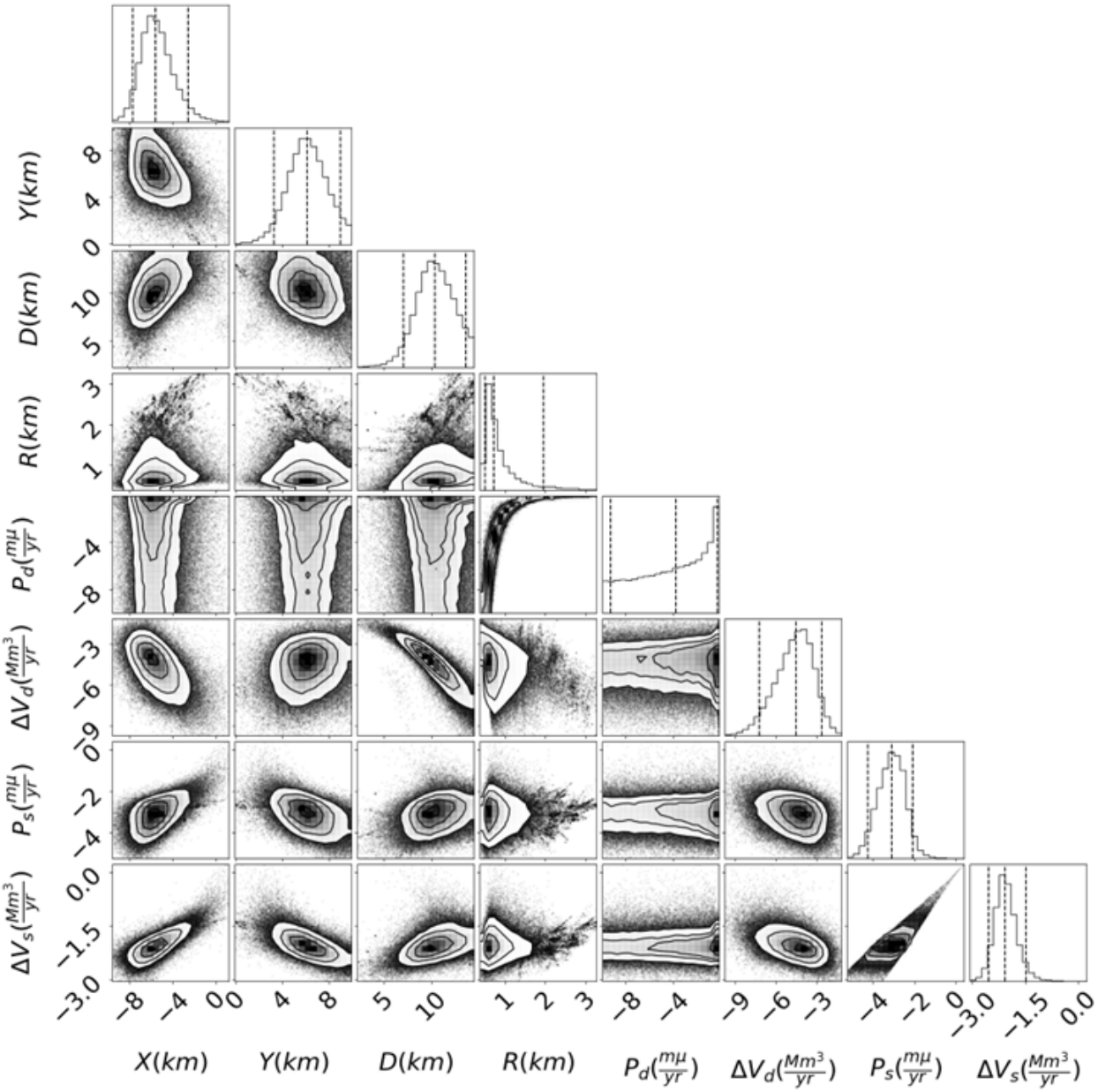

Fig. S13: Posterior distributions for the deflation episode between September 2022 and March 2024 and a dual spherical source model. The labels are the same as Figure S6. X, Y, D and R are associated with the deep source. The subindexes d, and s represent the deep and shallow sources, respectively.

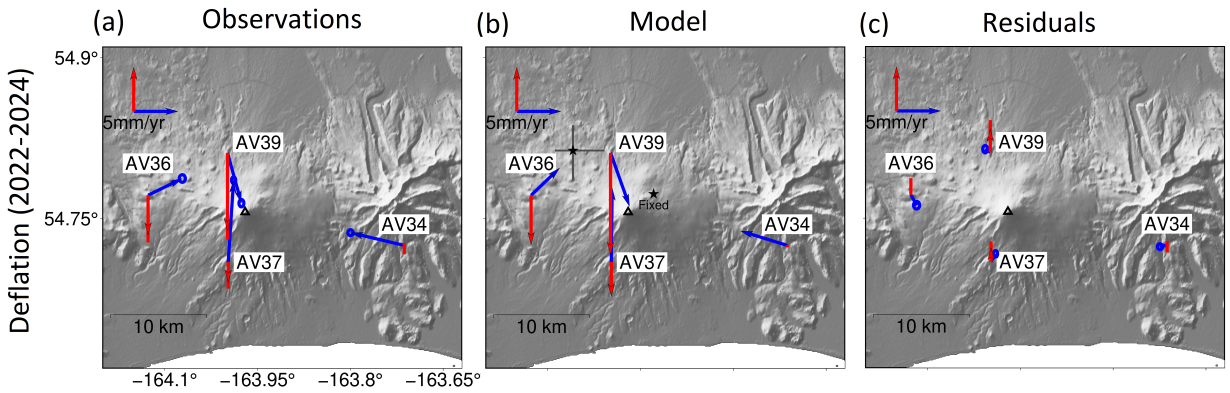

Fig. S14: Similar to Figure 6, but for deformation for the MAP solution from the inversion on the deflation episode using a dual-spherical source model. The stars represent the source locations and the lines the uncertainty in the horizontal location. Other symbols and labels are the same as in Figure 6.

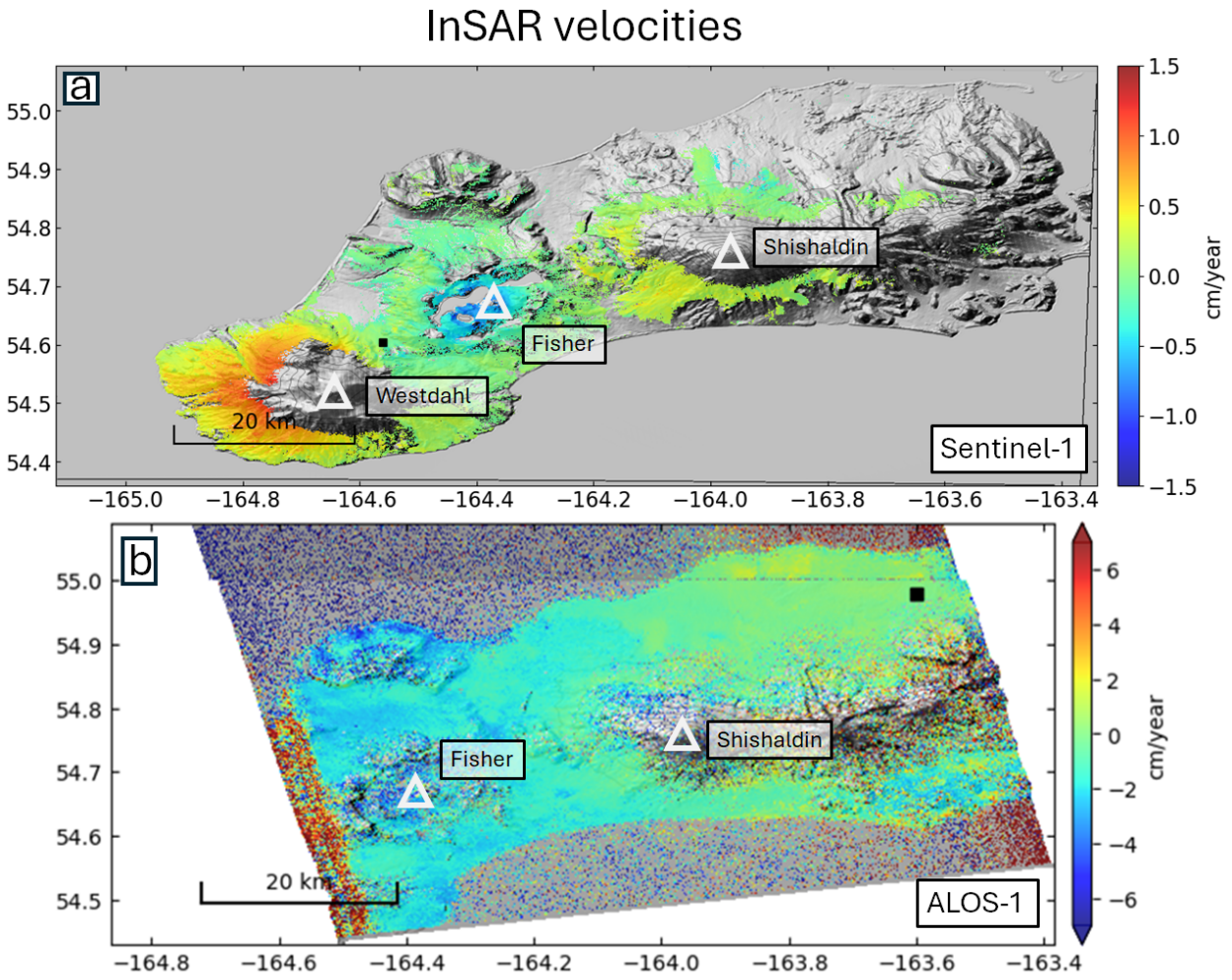

Fig. S15: InSAR line-of-sight (LOS) velocities using (a) Sentinel-1 from 2015 to 2021 and (b) ALOS-1 from 2007 to 2010. The colorbars are adjusted according to the wavelength of each Satellite mission (22.9 cm for ALOS-1 and 5.5 cm for Sentinel-1). The white triangles represent Westdahl, Fisher and Shishaldin. Deformation of Fisher and Westdahl have been reported on Angarita et al. (2024).

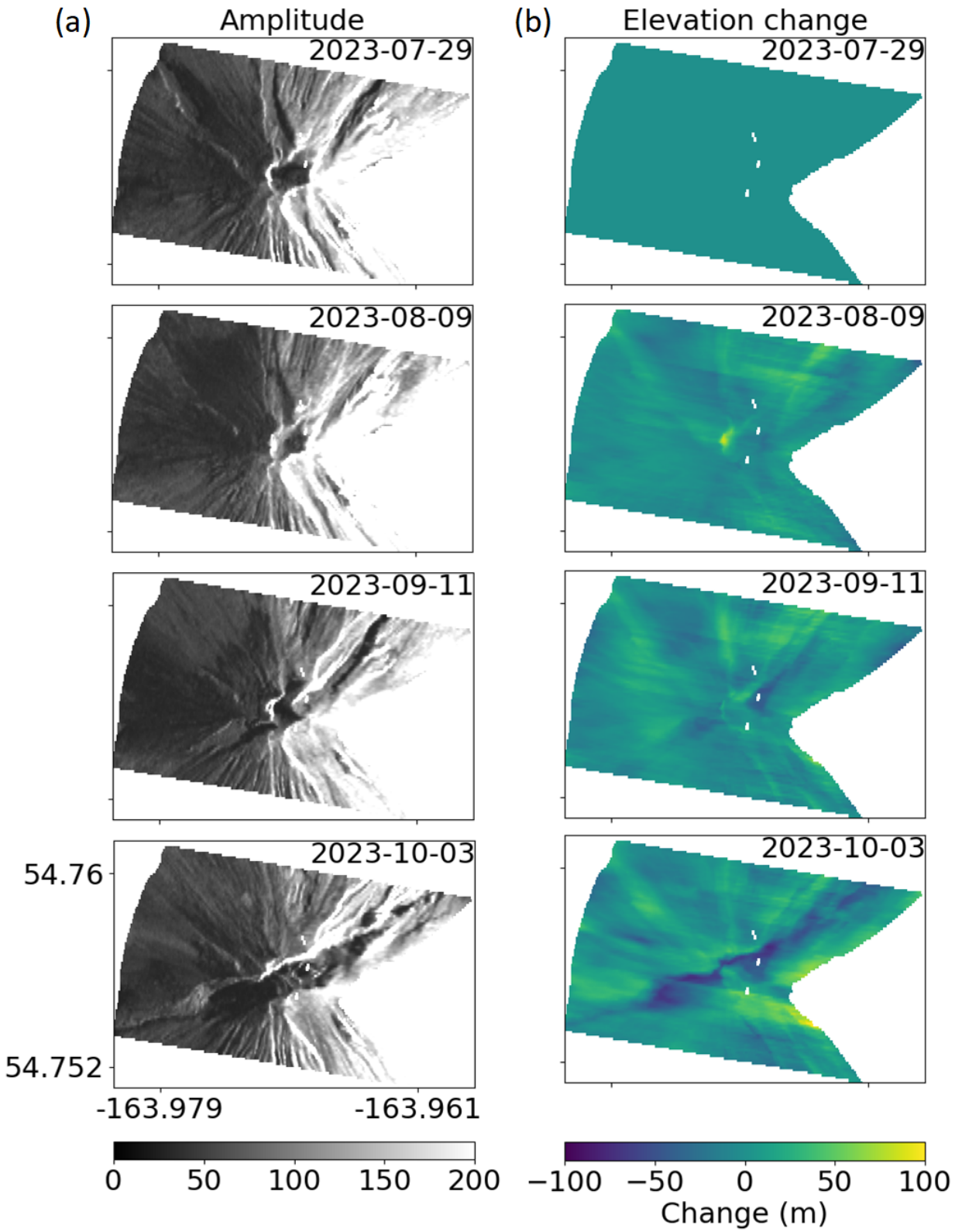

Fig. S16: Elevation changes for the 2023 eruption inferred from the amplitude of TerraSAR-X imagery. (a) Amplitude images showing Shishaldin vent between July 29 and October 03, 2023. (b) Inferred elevation changes taking as reference the elevation map from July 29, 2023.

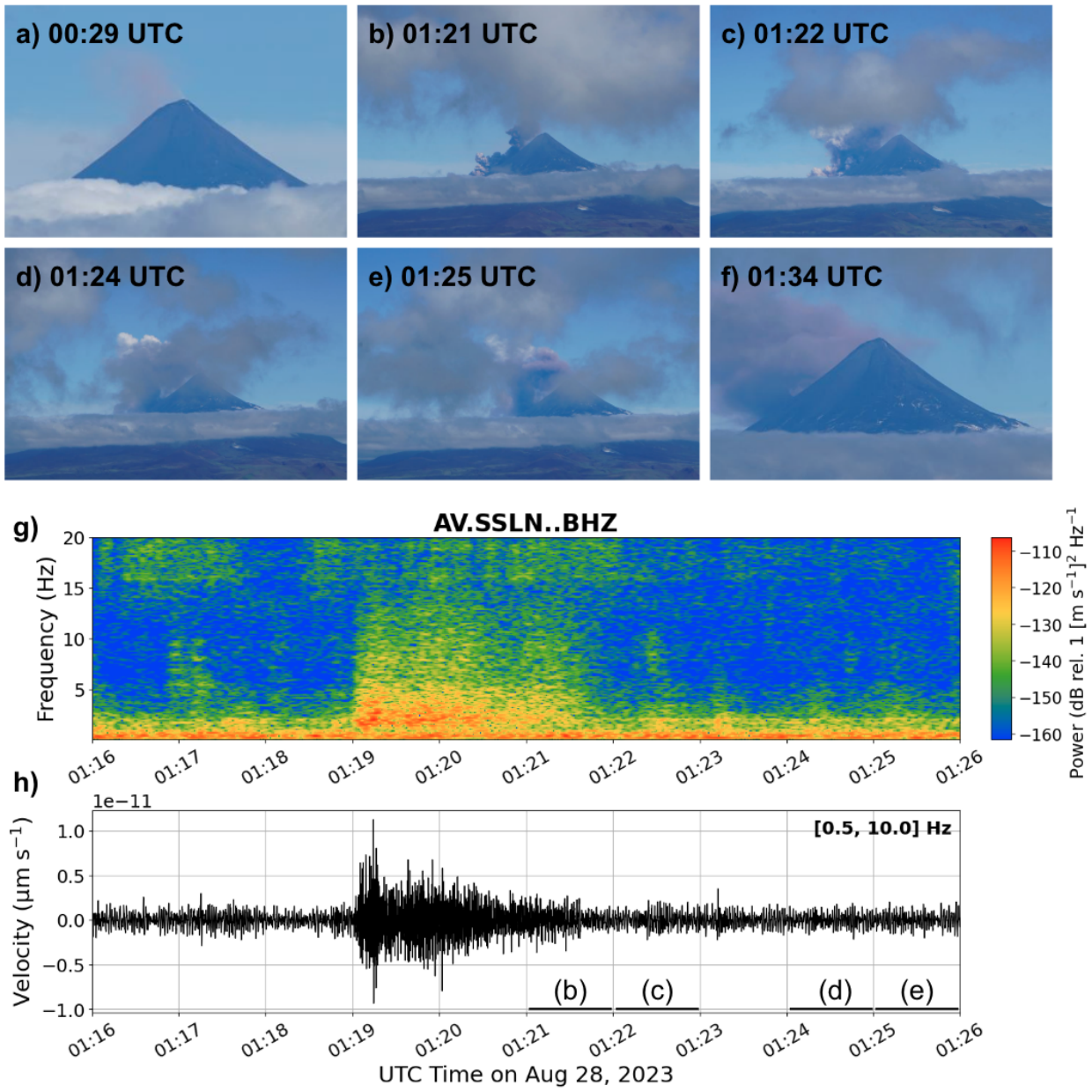

Fig. S17: Photo sequence documenting the rim collapse at Shishaldin on August 28, 2023. a)-f) Photographs taken by Darren Tan while conducting geophysical maintenance at WTUG (54.8466, -164.3873), 28.8 km WNW of Shishaldin. Images are cropped and zoomed to maintain a consistent perspective on the volcano. g) Seismic spectrogram from SSLN station data. h) Corresponding seismic waveform bandpass filtered between 0.5–10 Hz. The seismic signal begins at 01:19 UTC.

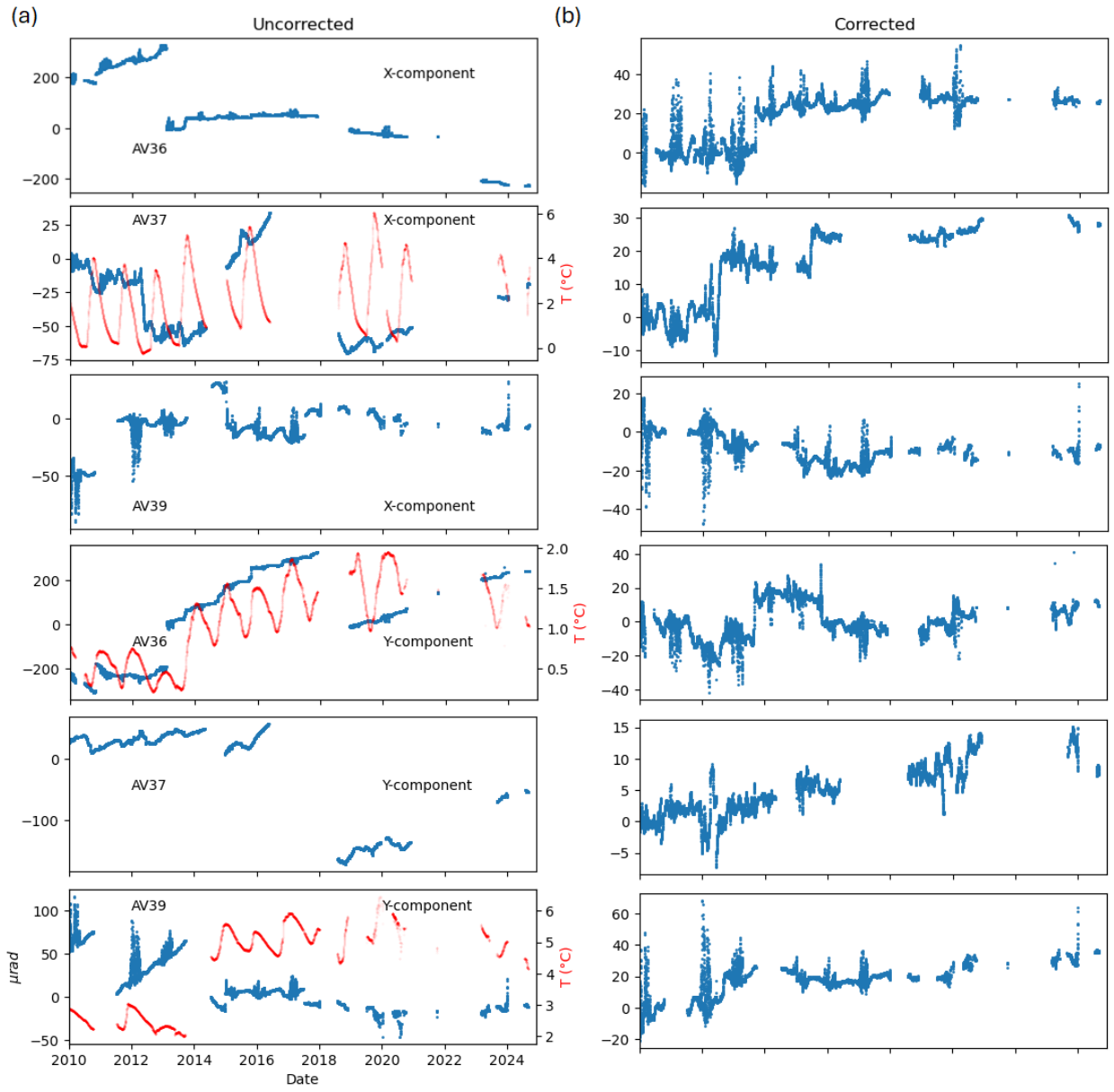

Fig. S18: Tilt timeseries and drift and thermal corrections. (a) Before corrections and (b) after thermal and drift corrections. The blue points represent the tilt observations and the values are given by the left-hand axes. The X-component are shown in the first three rows and the Y-components are shown in the last three rows. The red points show the tiltmeter temperatures and the values are shown in the right-hand axes.

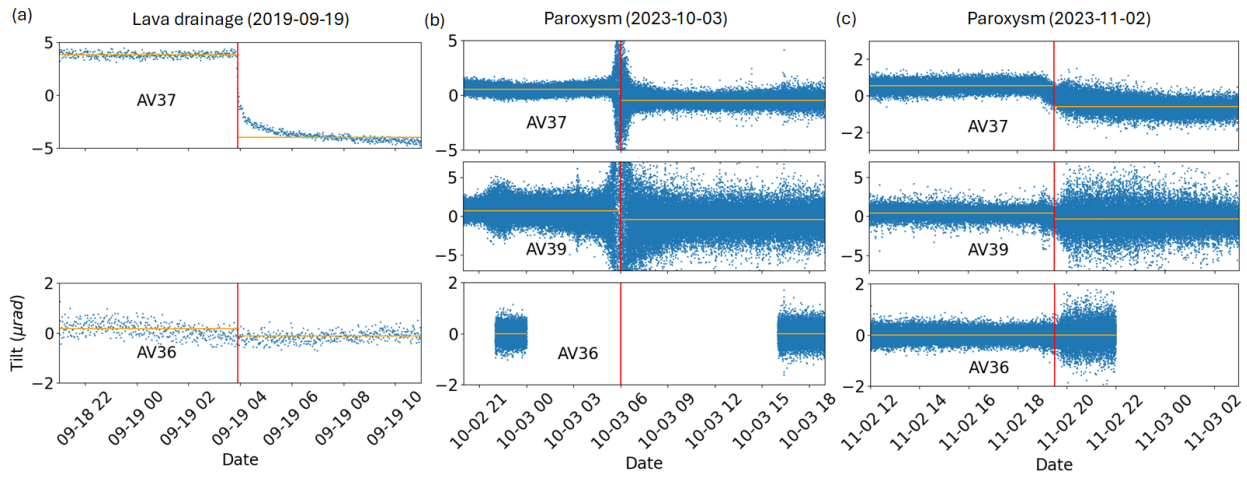

Fig. S19: Radial tilt displacements in response of volcanic events. (a) Lava drainage in September 19, 2019. (b) Paroxysm on October 3, 2023. (c) Paroxysm on November 2, 2023. The x-axis represent local time. The blue points are the tilt observations in microradians. The red line represents the event time and the orange line represents the median for the tilt observations before and after events.

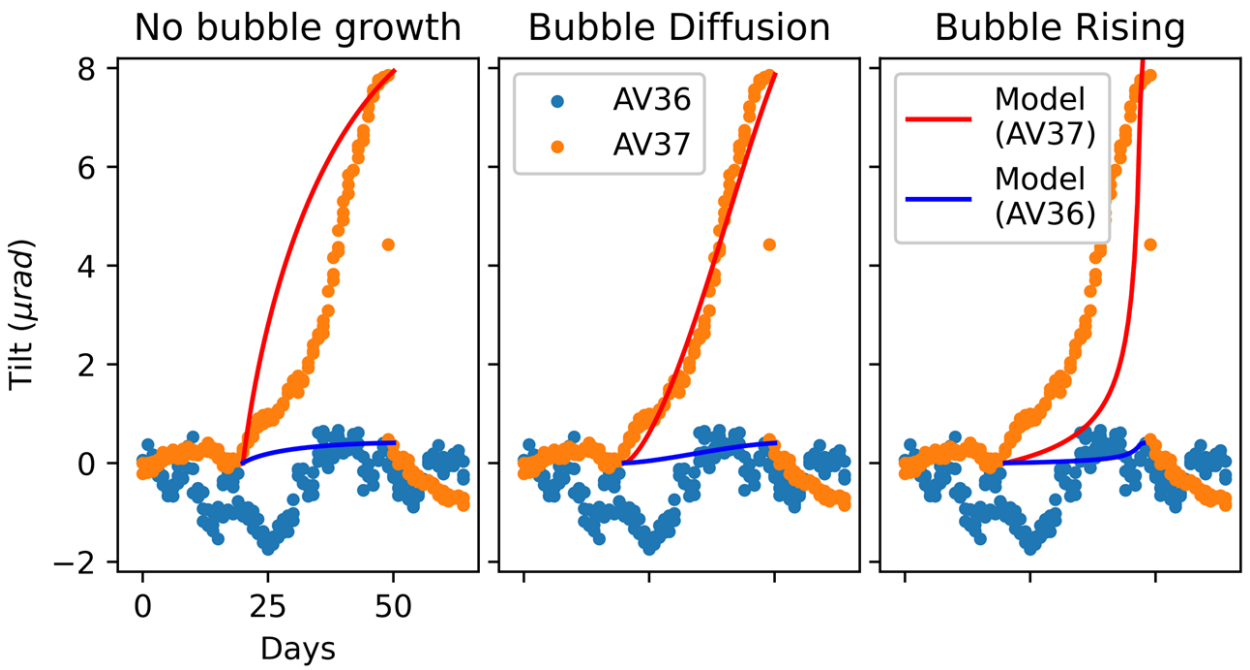

Fig. S20: Tilt time series for the lava drainage event and time dependent models for an open conduit for different magma dynamics: (a) Melt with bubbles that do not grow in size. (b) Melt with bubbles that increase their size due to mass transfer diffusion of water molecules. (c) Bubbles rise faster than the melt, allowing their volume to increase with decreased pressure. The blue and orange points represent the tilt observations at AV36 and AV37, respectively. The red and blue lines represent the time dependent forward models at AV36 and AV37, respectively.

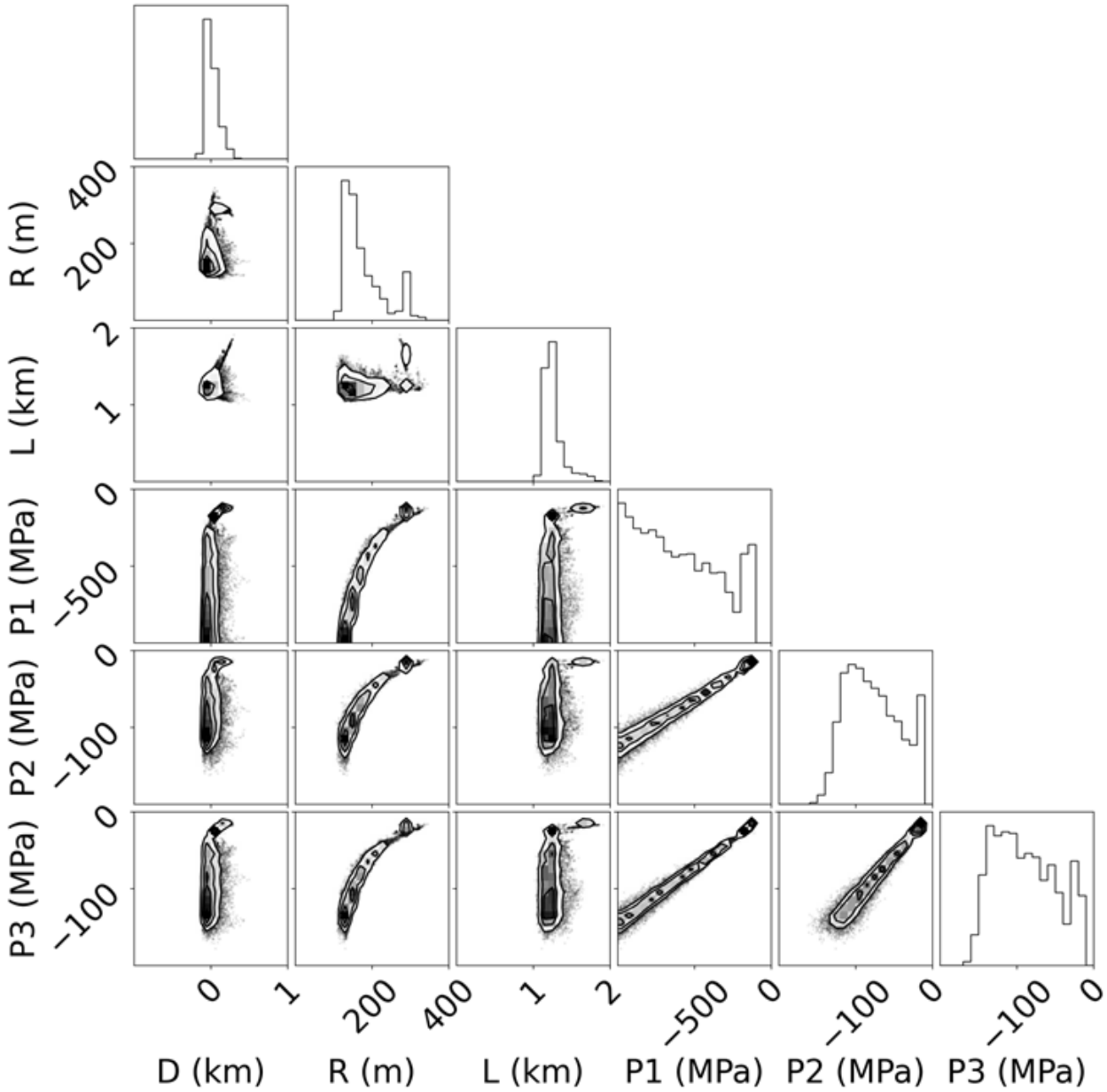

Fig. S21: Posterior distributions for the tilt displacements using the open conduit model. D represents the centroid depth, R the radius, L the length of the conduit, P1, P2 and P3 are the conduit pressure changes for the lava drainage event and the paroxysms on October, 3 and November 2, 2023 respectively.

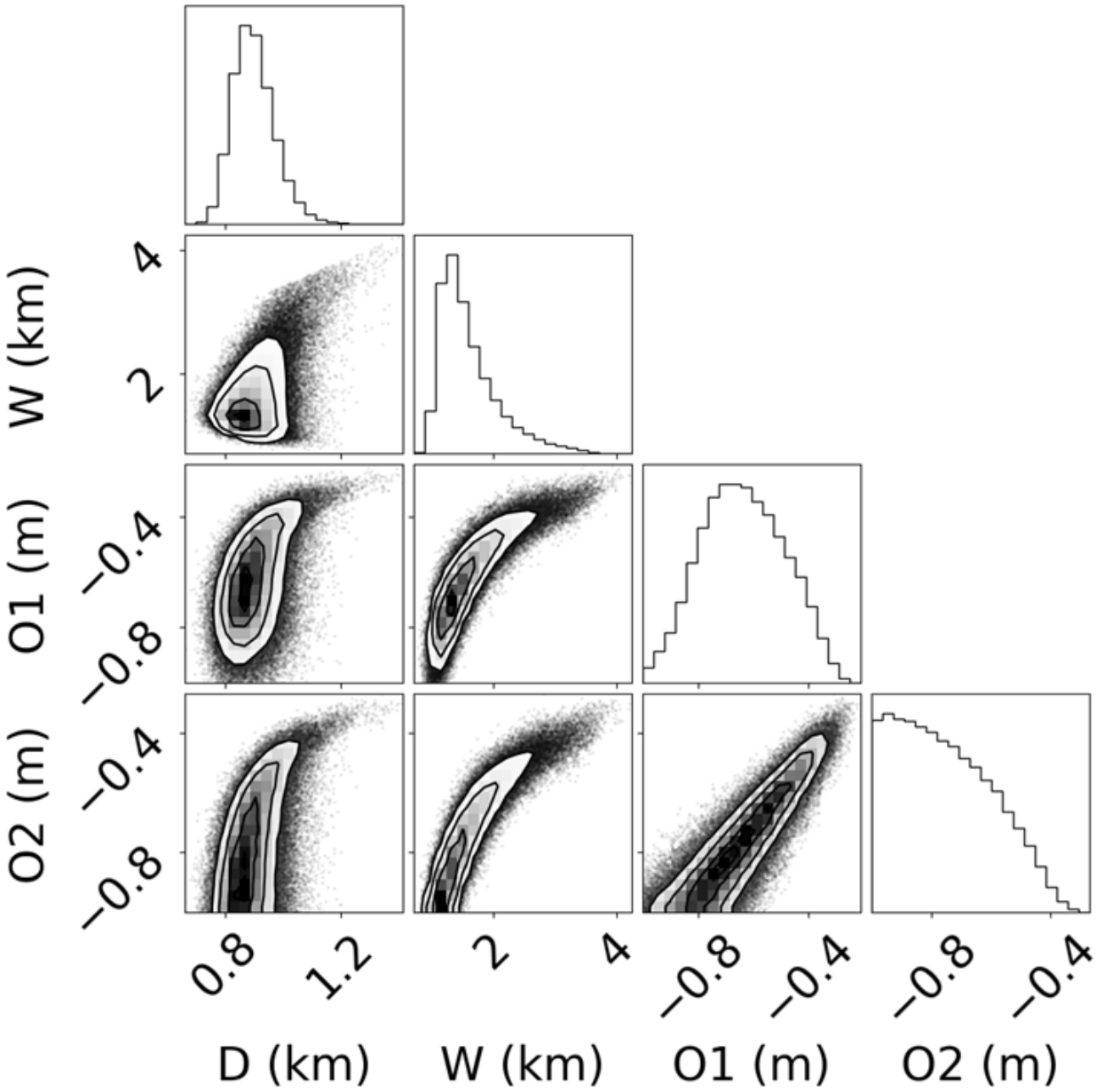

Fig. S22: Posterior distributions for the tilt displacements using the dike model. D represents the depth of the centroid, W and O, the dislocation width and opening, respectively. The indices 1 and 2 represent the paroxysms on October 3, and November 2, 2023 respectively.

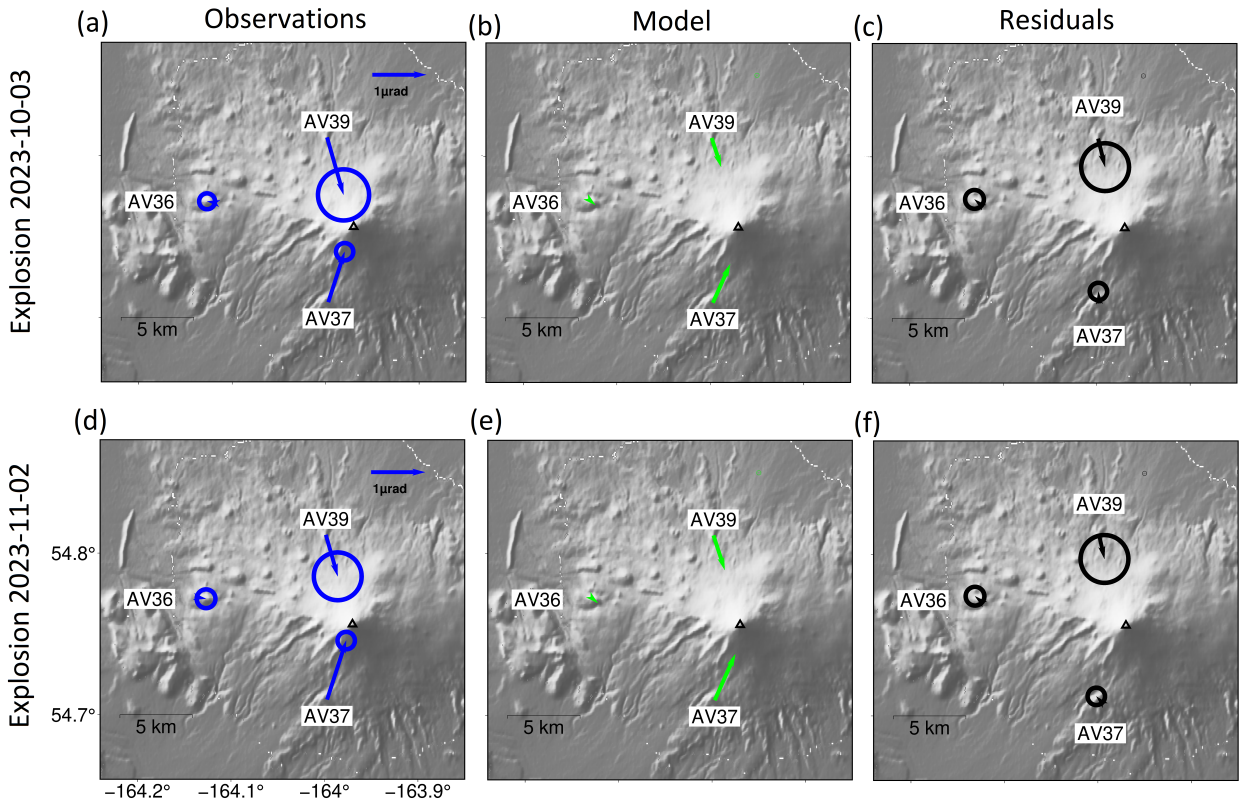

Fig. S23: Tilt displacements for the last two paroxysms in the 2023 eruption (a and d), modeled displacements using the dike implementation (b and e), residuals (c and f). Blue, green and black arrows represent the observations, model and residuals respectively. Circles represent the observation uncertainties.

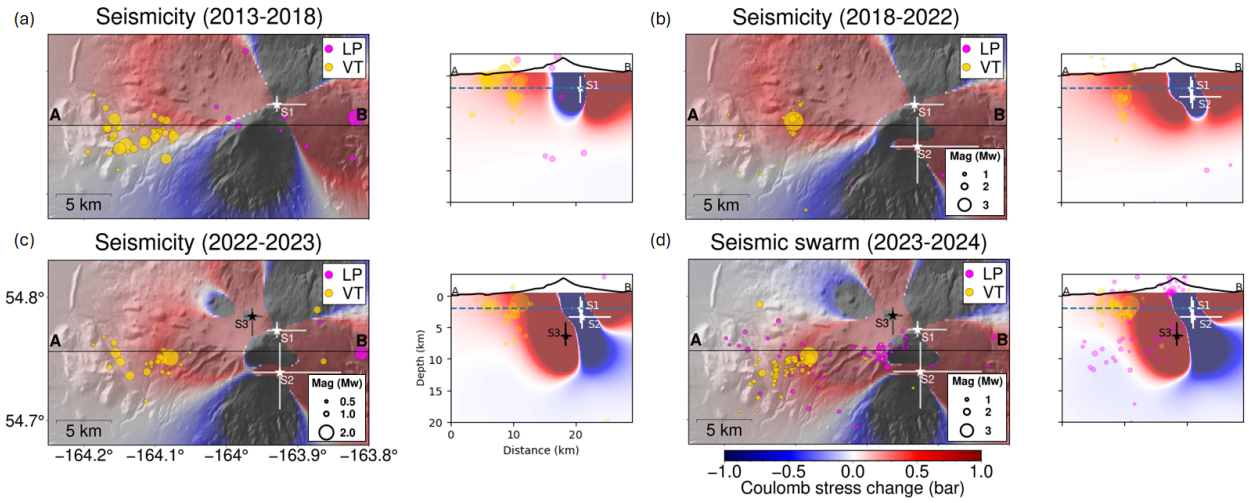

Fig. S24: Coulomb stress change for: (a) First inflation source and seismicity during February 1, 2013 and October 1, 2018. (b) First and second inflation sources and seismicity between October 1, 2018 and September 5, 2022. (c) Inflation sources and deflation source between the start of the deflation episode and the onset of the 2023 eruption and seismicity between September 5, 2022 and July 28, 2023. (d) Inflation and deflation sources and seismicity between July 28, 2023 and June 1, 2024. White and black stars represent inflation sources and deflation source respectively and white and black lines represent uncertainty for their locations.

References

Angarita, M., Grapenthin, R., Henderson, S., Christoffersen, M., and Anderson, K. R. (2024). Versatile Modeling Of Deformation (VMOD) inversion framework: Application to 20 years of observations at Westdahl volcano and Fisher Caldera, Alaska, us. *Geochemistry, Geophysics, Geosystems*, 25(4):e2023GC011341.

Girona, T., Realmuto, V., and Lundgren, P. (2021). Large-scale thermal unrest of volcanoes for years prior to eruption. *Nature Geoscience*, 14(4):238–241.

Lundgren, P., Girona, T., Bato, M. G., Realmuto, V. J., Samsonov, S., Cardona, C., Franco, L., Gurrola, E., and Aivazis, M. (2020). The dynamics of large silicic systems from satellite remote sensing observations: The intriguing case of domuyo volcano, argentina. *Scientific reports*, 10(1):11642.

Nishimura, T. (2009). Ground deformation caused by magma ascent in an open conduit. *Journal of Volcanology and Geothermal Research*, 187(3-4):178–192.

Reed, M. H., Munoz-Saez, C., Hajimirza, S., Wu, S.-M., Barth, A., Girona, T., Rasht-Behesht, M., White, E. B., Karplus, M. S., Hurwitz, S., et al. (2021). The 2018 reawakening and eruption dynamics of steamboat geyser, the world's tallest active geyser. *Proceedings of the National Academy of Sciences*, 118(2):e2020943118.

Zhan, Y., Le Mével, H., Roman, D. C., Girona, T., and Gregg, P. M. (2022). Modeling deformation, seismicity, and thermal anomalies driven by degassing during the 2005-2006 pre-eruptive unrest of augustine volcano, alaska. *Earth and Planetary Science Letters*, 585:117524.